Acta Materialia 281 (2024) 120424

Contents lists available at ScienceDirect

Acta Materialia

journal homepage: www.elsevier.com/locate/actamat

Full length article

Insights into irradiation-affected structural evolution and mechanical behavior of amorphous carbon

Yeran Shi [a], Qiaosheng Xia [a], Mingda Xie [a], Qing Zhou [a,*], Dongpeng Hua [a], Liqiang Chai [b], Tan Shi [c], Stefan J. Eder [d,e,*], Haifeng Wang [a,*], Peng Wang [b], Weimin Liu [a,b]

[a] Center of Advanced Lubrication and Seal Materials, Northwestern Polytechnical University, Xi'an, Shaanxi 710072, PR China
[b] State Key Laboratory of Solid Lubrication, Lanzhou Institute of Chemical Physics, Chinese Academy of Sciences, Lanzhou 730000, PR China
[c] School of Nuclear Science and Technology, Xi'an Jiaotong University, Xi'an 710049, PR China
[d] Institute for Engineering Design and Product Development, TU Wien, Lehárgasse 6 - Objekt 7, Vienna 1060, Austria
[e] AC2T research GmbH, Viktor-Kaplan-Straße 2/C, Wiener Neustadt 2700, Austria

ARTICLE INFO

Keywords:
Amorphous carbon
Irradiation
Nanomechanical behavior
Molecular dynamics simulation

ABSTRACT

The distinctive hybridization structure of amorphous carbon (a-C) imparts remarkable mechanical and tribological characteristics, making it highly relevant for lubrication applications, particularly in critical sectors such as nuclear energy. In this work, we employed molecular dynamics simulations to examine the effects of irradiation on the structural evolution and mechanical behavior of a-C. The findings indicate that with increasing irradiation doses, the short-range order within the a-C is disrupted, leading to a substantial increase in sp^2 hybridization. Then, nanoindentation simulations revealed a reduction in both hardness and elastic modulus as a consequence of irradiation damage, associated with the transition in hybridization from sp^3 to sp^2 and the associated creation of free volume. Furthermore, nanoscratch mechanical testing showed a slight increase in the friction, primarily attributed to the weakened load-bearing ability of a-C after irradiation. Interestingly, a metastable transition from sp^2 to sp^3 hybridization was observed on the scratched surface, which was concurrently validated by experiments as Raman spectroscopy and TEM-EELS. This study provides a detailed atomic-level mechanism for the irradiation-induced damage on the structural bonding and mechanical properties of a-C, offering guidance for its performance in nuclear reactors and the aerospace industry.

1. Introduction

Amorphous carbon (a-C) refers to a type of amorphous carbon material characterized by a mixture of sp^2 and sp^3 hybridized carbon atoms [1,2]. The distinct microstructural features and bonding configurations of a-C merge the lubrication characteristics of sp^2-hybridized carbon with the mechanical strength of sp^3- hybridized carbon [3,4]. This amalgamation opens up wide-ranging possibilities for the utilization of a-C in tribological applications, especially in critical environments such as extreme temperature [5,6], vacuum [7], irradiation [8], etc.

The rapid expansion of nuclear energy in recent decades has resulted in a significant demand for solid lubricants to be used in mechanical components within nuclear facilities. a-C, as a remarkable option, has found applications in plasma-facing material [9], rocker shaft and roller pin [10], etc. Irradiation within nuclear reactors is a key element contributing to the deterioration of material performance. Currently, research endeavors are dedicated to investigating the frictional performance of a-C coatings, both prior to and after irradiation. Xu et al. [11] conducted Ni ion irradiation experiments on a-C to investigate the morphology as well as the mechanical and tribological properties of the film. It was found that the local sp^3-sp^2 transformation in the irradiation area is an important factor leading to rapid failure of the lubrication performance of the irradiated thin film. Shen et al. [12] found that Ni ion implantation can reduce the wear resistance of a-C and cause delamination upon friction. Nevertheless, up to this point, the majority of existing research has not thoroughly examined the influence of the irradiation dose on the mechanical characteristics of a-C, nor has it aimed at clearly understanding the mechanisms behind the deterioration in wear resistance of thin films.

A thorough investigation into the evolution of bonds, the energy transfer dynamics during irradiation, and the interactions between incoming and matrix atoms is essential to gain a deeper insight into the

* Corresponding authors.
E-mail addresses: zhouqing@nwpu.edu.cn (Q. Zhou), stefan.j.eder@tuwien.ac.at (S.J. Eder), haifengw81@nwpu.edu.cn (H. Wang).

https://doi.org/10.1016/j.actamat.2024.120424
Received 30 July 2024; Received in revised form 17 September 2024; Accepted 20 September 2024
Available online 21 September 2024

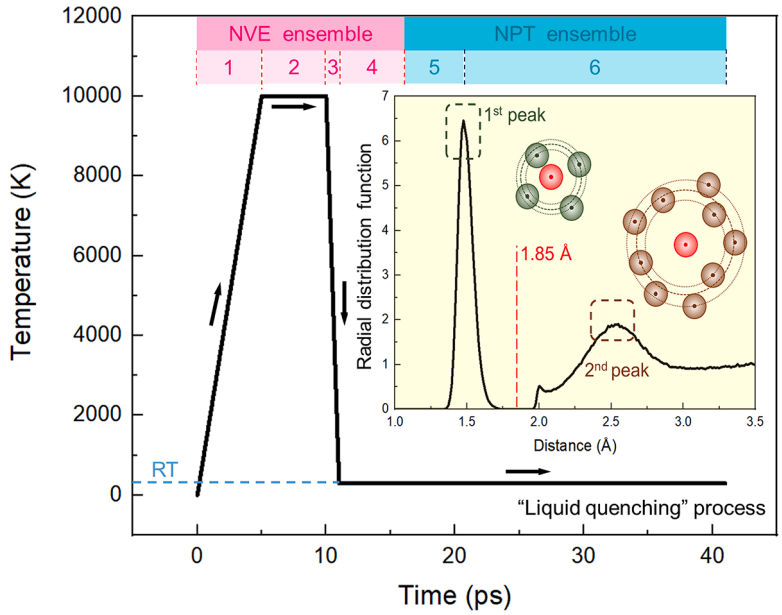

Fig. 1. Process diagram of a-C model generation. The figure includes four steps in the NVE ensemble: heating, maintaining at 10,000 K, cooling, and maintaining at 300 K, and two steps in the NPT ensemble: relaxation in PPP (X-Periodic, Y-Periodic, Z-Periodic) and relaxation in PPS (X-Periodic, Y-Periodic, Z-"shrink wrapped"). The inset is the radial distribution function of the model.

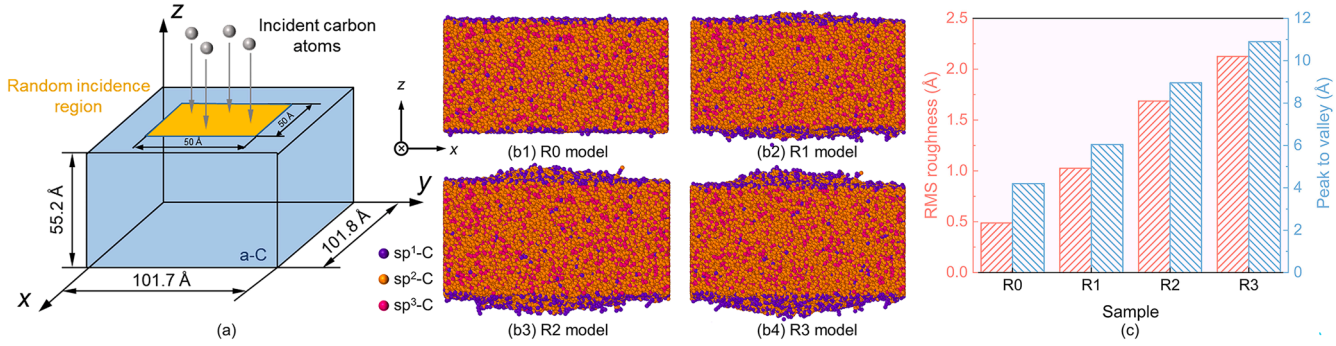

Fig. 2. Schematic diagram of the irradiation process: (a) Irradiation model; (b) The overall morphology under different irradiation doses (The radiation doses of R0, R1, R2, R3 are 0 atoms/cm^2, 4·10^{14} atoms/cm^2, 8·10^{14} atoms/cm^2, and 12·10^{14} atoms/cm^2, respectively); (c) Statistics of RMS roughness (pink) and R_z (blue) for each sample after irradiation. (For interpretation of the references to colour in this figure legend, the reader is referred to the web version of this article.)

possible damage mechanisms of a-C. The constraints imposed by temporal and spatial resolution often hinder the direct observation of these processes experimentally. Employing molecular dynamics (MD) simulations offers a practical approach to overcome these challenges [13-16]. The simulation of friction processes involving a-C has consistently been a highly popular research area [17-19]. Wang et al. [20] conducted molecular dynamics simulations to study the friction mechanism at the friction interface and the hybridization transformation in the bonding structure of a-C coatings. Li et al. [21] examined how the frictional performance of a specially designed a-C system correlates with sliding velocity and contact pressure via reactive molecular dynamics simulations. They found that changes in the interface structure from sp^3 to sp^2 bonds are more influenced by contact pressure than by sliding speed, highlighting the greater impact of mechanical stress over kinetic factors in this context. However, the state of research on the irradiation effect and mechanical behavior of a-C coatings is limited, with the majority of studies concentrating on the swift heavy ion model [22,23].

Given the outlined circumstances, this research delves into the typical behavior of irradiated a-C with a density of 2.8 g/cm^3, employing molecular dynamics (MD) simulations to particularly assess bonding and structural evolution. Furthermore, our study meticulously examines the impact of irradiation on nanomechanical properties and the deterioration of tribological characteristics, shedding light on the intrinsic connection between structure and properties. By compiling these findings, this study not only advances our understanding of how irradiation influences the performance of a-C, but also lays a foundation for further research and practical applications of a-C in the nuclear industry.

2. Simulation method

Carbon atoms are initially dispersed using the Packmol package [24]. All simulations are conducted using the Large-scale Atomic/Molecular Massively Parallel Simulator (LAMMPS) [25]. The obtained simulation data is visualized with the Open Visualization Tool (OVITO) [26].

2.1. Modeling

In preparation, we used the Packmol package to randomly disperse 80,000 carbon atoms into a 100 Å × 100 Å × 50 Å box, which is much larger than the size of the main cascading collision zones. The "liquid quenching" method [27] is chosen to construct the a-C atomic model,

which has been proven to accurately reproduce the experimentally observed characteristics of a-C. Periodic boundary conditions are used in the *X, Y,* and *Z* directions, and the melting and quenching processes are simulated in the micro-canonical (NVE) ensemble. The time step was 0.1 fs in all simulations. The temperature is controlled using the "temp/rescale" method. According to Hilbert et al.'s work [28], the model construction process involves the following specific steps (Fig. 1): (1) Increase temperature from 0.1 K to 10,000 K within 5 ps; (2) Maintain temperature at 10,000 K for 5 ps; (3) Reduce the temperature to 300 K within 1 ps; (4) Maintain temperature at 300 K for 5 ps; (5) Maintain 300 K and 0 GPa external pressure under the isothermal–isobaric (NPT) ensemble via Nose-Hoover thermostat/ barostat for 5 ps; (6) Change the periodic boundary conditions in ± *Z* to free boundaries to generate a free surface, and relax the free surface by running 20 ps in the NPT ensemble to create an environment suitable for the bombardment process. As a result, we have successfully established an a-C atomic model with a density of 2.8 g/cm^3. The radial distribution function (RDF) reveals a first peak positioned approximately at 1.54 Å [29], a second "pseudo peak" around 2.1 Å resulting from the cutoff of the potential [30], and a third, broad peak located around 2.52 Å signifying a pronounced structure with short-range order and long-range disorder (Fig. 1 inset). We selected a cutoff distance of 1.85 Å between the two main peaks to determine the coordination number.

For the irradiation simulation, the incident carbon atom is positioned above the central square (50 Å x 50 Å) within the model, carrying an initial kinetic energy of 5 keV (Fig. 2(a)). The choice of carbon atoms rather than ions is based on the knowledge that energy transfer is primarily governed by nuclear collisions with low kinetic energies, thereby allowing electronic interactions to be neglected [31]. The irradiation process (cascade overlapping) is carried out using a variable time step between 0.000001 fs and 0.5 fs to control the movement of atoms. The continuous incidence of carbon atoms is simulated in the NVE ensemble, and system stability is reached after 30,000 steps. The thermal energy generated by irradiation is then absorbed using the Berendsen temperature control method to maintain 300 K. The models where 100, 200, and 300 carbon atoms randomly impinge on the surface are labeled as R1, R2, and R3, respectively, while the unirradiated sample is designated as R0.

For nanoindentation simulations, the R0-R3 samples are structured into three distinct layers: a fixed layer occupying the bottom 5 Å, followed by a 5 Å thick temperature control layer positioned directly above, and a Newtonian layer of approximately 45 Å up to the surface [32]. A diamond indenter of 20 Å radius is pressed into the sample at a velocity of 20 m/s to a depth of 15 Å, held in place for 100 ps, and subsequently retracted at the initial velocity. For nanoscratch simulations, we replicate the irradiated model once along the x-direction. A diamond indenter with a radius of 15 Å is pressed into the sample to a depth of 10 Å and moved along the x-direction for 160 Å at a speed of 20 m/s.

2.2. Interatomic potential

To precisely model the carbon atom interactions in this work, we selected the Tersoff potential [33,34], which has been extensively employed for simulations of a-C with relatively high-density (>2.6 g/cm^3) [35,36]. Nevertheless, the Tersoff potential encounters challenges in accurately characterizing atom collisions at close proximity during irradiation events. Consequently, we smoothly connected the Ziegler-Biersack-Littmark (ZBL) universal repulsive potential [37] to describe the interaction at close range using the Fermi function, which predominantly controls the collision process [38,39]. The "distance-potential energy" curve is included in the Supplementary Materials. In addition, we selected the Lennard-Jones (LJ) potential to describe the van der Waals (vdW) interactions between the carbon atoms in the diamond indenter and the carbon atoms in the a-C matrix during nanoindentation and the nanoscratch processes [33], with a depth of the potential well $\varepsilon = 0.00284$ eV and a zero-crossing distance $\sigma = 3.4$ Å [40]. The diamond indenter is modeled as a rigid body, therefore its internal interactions are neglected.

3. Material and methods

Thin a-C films were prepared on the surface of single-crystal silicon substrates using magnetron sputtering [11] with a supply power of 1.8 ± 0.2 kW and a deposition time of 100 min. The total thickness of the prepared carbon film was approximately 1.5 μm. The sample then underwent carbon ion irradiation at a dose of ~10^{15} ions/cm^2. A single-pass scratch was performed on the irradiated as well as the unirradiated reference samples using a tribometer (UMT Tribo, Bruker, USA) with a normal force of 3 N. The surface morphology was examined via Scanning Electron Microscopy (SEM, Supra 55, Zeiss, Germany), and the hybridization states of carbon were analyzed using Raman spectroscopy (Alpha 300R, WITec, Germany) with wavelength of 532 nm. To prepare thin lamellae of the scratched scar for transmission electron microscopy (TEM, FEI Talos F200X, USA) observation, a focused ion beam (FIB) system (FEI Helios G4 CX, USA) was utilized, electron energy loss spectroscopy (EELS) is captured by double Cs-corrected TEM (FEI Themis Z, USA).

4. Results and discussion

4.1. Irradiation simulations

4.1.1. Radiation-induced morphological changes

Based on the a-C model established in Section 2.1, as shown in Fig. 2 (b1), we observe that carbon atoms exhibiting sp^1 hybridization are predominantly located on the surface [29]. The bulk structure of the model comprises a mixed hybridization of sp^2 and sp^3 carbon atoms, with the precise ratios detailed in the subsequent text. Besides, the bulging of the central region can be obviously observed in Fig. 2(b) as a result of the irradiation effect. To be more quantitative, we use the Alpha-shape method [41] to extract atoms from the surface of the model for roughness analysis. The root-mean-square (RMS) roughness is given as follows:

$$S_q = \sqrt{\frac{1}{N}\sum_{i=1}^{N}(Z_i - \overline{Z})^2} \tag{1}$$

where S_q is the RMS roughness, N stands for the number of surface atoms, Z_i is the position in Z direction of the i th atom and $\overline{Z}$ is the average position in Z direction of all surface atoms. Fig. 2(c) suggests that radiation can cause a significant increase in surface roughness of a-C, as confirmed by experiments [11]. Also, an increase in irradiation dose is accompanied by an increased surface roughness. Another approach to assessing surface roughness involves measuring the height difference between the highest peak and the deepest valley (R_z), quantifying the height of the irradiated protuberance. This quantity exhibits a trend consistent with that observed in the RMS roughness data.

4.1.2. Structural changes caused by irradiation

Irradiation typically changes the stress state of materials. Therefore, we calculated the average biaxial stress of a-C atoms during the irradiation process, using the following formulas [42]:

$$P_{IJ} = \frac{\sum_k^N m_k v_{kI} v_{kJ}}{V} + \frac{\sum_k^N r_{kI} f_{kJ}}{V} \tag{2}$$

$$P = \frac{1}{3}\left[P_{xx} + P_{yy} + P_{zz}\right] \tag{3}$$

$$\sigma = -\frac{3}{2}P \tag{4}$$

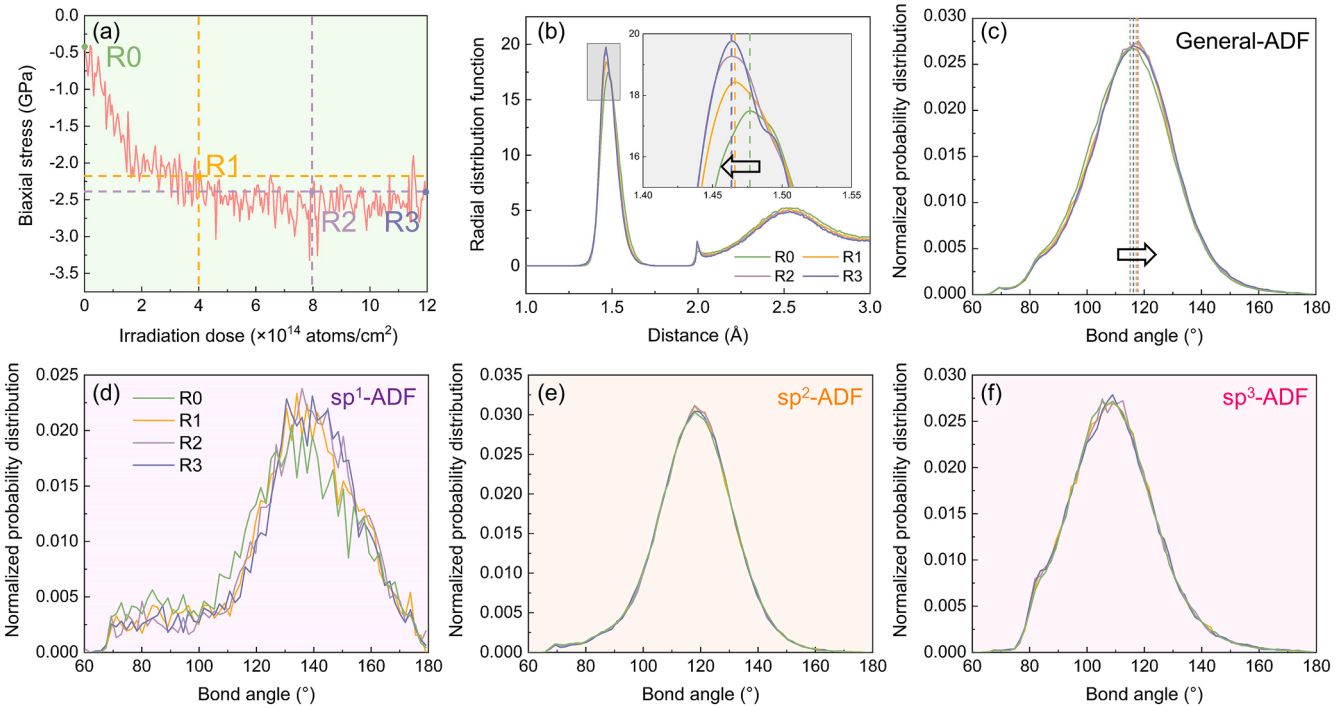

Fig. 3. Changes in biaxial stress, bond length, and bond angle in models with different irradiation doses: (a) Relationship between biaxial stress and irradiation dose, continuously recorded during the irradiation process; (b) radial distribution function for each model, the inset shows an enlarged view of the peak ranging from 1.4 to 1.55 Å; (c) General angle distribution functions (ADF) for the four models, demonstrating the changes in bond angle caused by irradiation; (d-f) ADF diagrams for the different hybridization states (sp^1, sp^2, sp^3) of carbon atoms. The R0-R3 samples are represented by green, yellow, purple, and navy, respectively. (For interpretation of the references to colour in this figure legend, the reader is referred to the web version of this article.)

Here, I and J take on values x, y and z; k is the kth atom in the domain; N is the total number of atoms in the sample; m_k is the mass of atom k; v_{kI} and v_{kJ} are the Ith and Jth components of the velocity of atom k; V is the volume of the sample; r_{kI} is the Ith component of the position of atom k; f_{kJ} is the Jth component of the force applied on atom k; P represents hydrostatic pressure; P_{xx}, P_{yy}, and P_{zz} denote components of stress tensors in the X, Y, and Z directions, respectively; σ represents biaxial stress, the factor of 1.5 is according to McKenzie [43,44]. The calculation results are shown in Fig. 3(a). The observation indicates that a-C initially exhibits negative biaxial stress, commonly referred to compressive stress in the unirradiated sample. With increasing irradiation doses, there is a substantial rise in the compressive stress, which then appears to stabilize after reaching a certain threshold, consistent with experiments [45]. The compressive stress induced by irradiation shortens the carbon-carbon covalent bond length, leading to a leftward shift of the first peak in the RDF. Nevertheless, the bond length in the R1-R3 samples remains relatively unchanged, attributed to the similarity of compressive stresses in these three samples (Fig. 3(b)). The slight increase in bond angle, as indicated by Fig. 3(c), is mainly attributed to the difference in bond angles between sp^2 and sp^3 (120° *vs.* 109.5°). Radiation causes a transition of carbon atom hybridization from sp^3 to sp^2, resulting in an increase in the general angle distribution function (ADF). The ADF diagrams for the different hybridizations of carbon atoms are further provided in Fig. 3(d)–(f). It can be seen that the bond angles for sp^1 hybridized carbon undergo significant changes after irradiation, whereas those for sp^2 and sp^3 carbon atoms remain relatively stable. This stability in sp^2 and sp^3 hybridized carbon bond angles suggests that the structural changes induced by irradiation are dependent on the hybridization state.

The atomic arrangements of a-C can be characterized using a Voronoi tessellation method [46], which is commonly employed for the analysis of amorphous materials [47]. As shown in Fig. 4(a), in all four models, the prevalence of 15–17–sided polyhedra is evident. However, with increasing irradiation doses, there is a decrease in the proportion of 15–17–sided polyhedra, while polyhedra with more than 20 (or fewer than 14) faces are created. This trend gradually diminishes, leading to a diverse evolution in face distributions across more or fewer directions, which can also be clearly seen from the Gaussian fitting of Fig. 4(a). Here, the abscissa of the Gaussian peaks in the four models remains almost unchanged, but the peaks decrease with the irradiation dose. On the other hand, Fig. 4(b) analyzed the number of edges on the face of the Voronoi polyhedra. In the unirradiated model, the optimal distribution of the 3-fold and 4-fold faces is evident. With an increase in irradiation dose, this preference is weakened and replaced by an increase percentage in 5–7-fold faces. the decrease in peak value of Gaussian fitting curve can also clarify this point. Furthermore, we use the parameter introduced by Kim et al. [48] to characterize the degree of spatial non-uniformity of carbon atoms distribution as follows:

$$h = \frac{1}{2N}\sum_{k=1}^{r} 8.89^{1-k}\sum_{i=1}^{2^{3k}}\left|m_i - \overline{m}(2^{3k})\right| \tag{5}$$

where h is the local inhomogeneity parameter. The closer the value is to 1, the more the atoms are clustered together. N represents the number of atoms, r is the smallest integer that satisfies $2^{3r} > N$, m_i is the number of atoms contained in each grid element, and $\overline{m}$ is the average of m_i. As shown in Fig. 4(c), the value of h increases with the irradiation dose, revealing an uneven spatial distribution of carbon atoms after irradiation. The above data all indicate that irradiation induces the gradual destruction of the short-range ordered structure of carbon atoms in a-C and intensifies amorphization. Fig. 4(d) shows the variation in free volume for the four models. As the irradiation dose increases, the free volume gradually increases, indicating a transition from a soild-like state to a liquid-like state. The increase in free volume enhances the material's plasticity, which will be discussed in detail in the following sections.

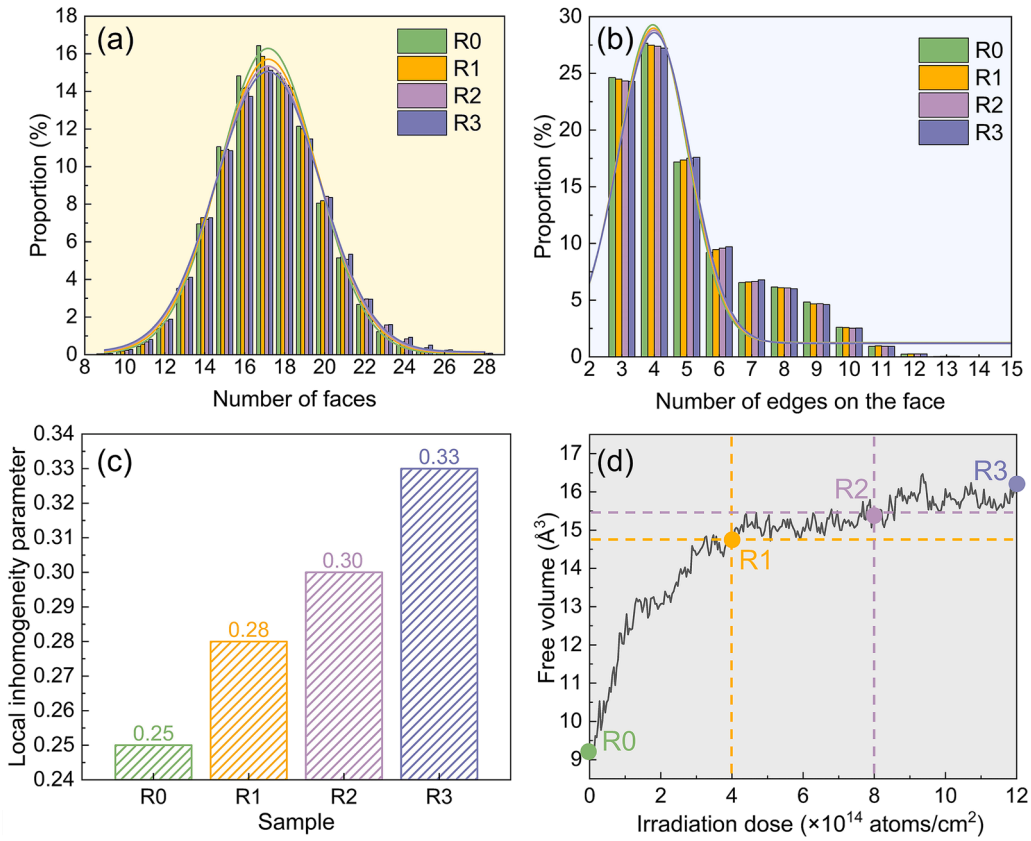

Fig. 4. Structural parameter change in a-C after irradiation: (a) Change in the number of Voronoi polyhedron faces, curves in the figure are Gaussian fits corresponding to the color of the bar charts; (b) Change in the number of Voronoi polyhedron edges, curves in the figure are Gaussian fits corresponding to the color of the bar charts; (c) Change in the local inhomogeneity parameter; (d) The increase in free volume caused by irradiation. The R0-R3 samples are represented by green, yellow, purple, and navy, respectively. (For interpretation of the references to colour in this figure legend, the reader is referred to the web version of this article.)

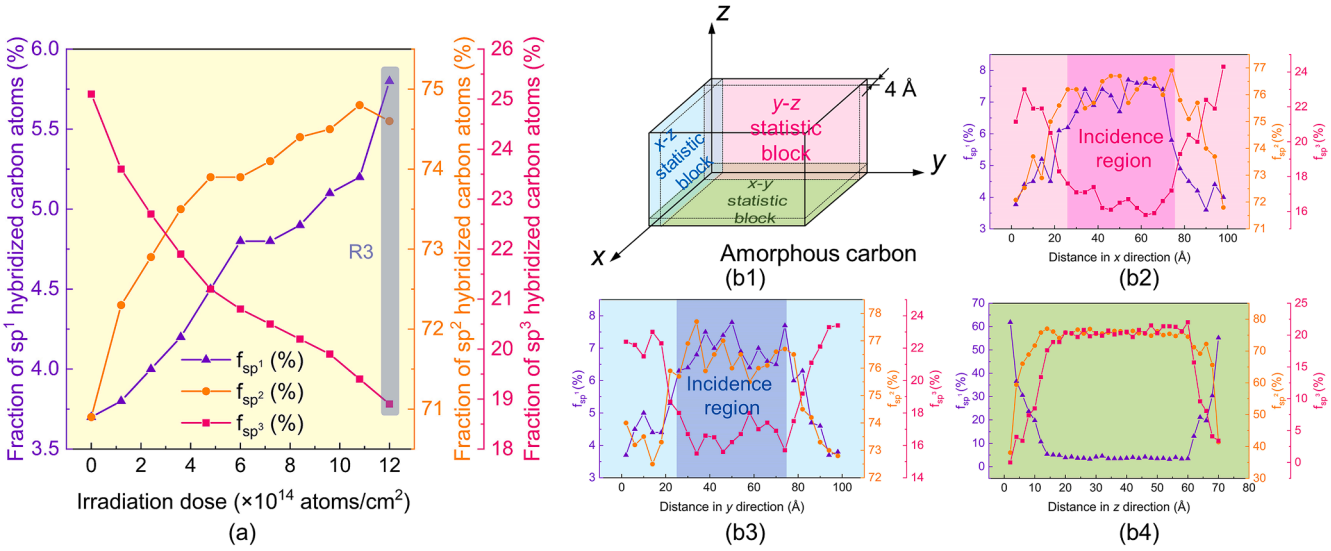

Fig. 5. Changes in hybridization state upon irradiation: (a) The evolution of hybridization structures with irradiation dose; (b1) Statistical block division on three directions for hybridization within a-C, the statistical block is divided into three directions, corresponding to the following (b2)-(b4); (b2-b4) Statistic of hybridization state along the x,y and z direction separately. The content of sp^1, sp^2 and sp^3 are represented by purple, orange and pink, respectively. (For interpretation of the references to colour in this figure legend, the reader is referred to the web version of this article.)

4.1.3. Radiation induced structure changes

In the initial model, sp^2 hybridized carbon accounted for around 70.9% of the total content, while sp^3 and sp^1 hybridized carbon constituted approximately 25.2% and 3.8% (Fig. 5(a)), respectively. Radiation can cause a large amount of transition from sp^3 to sp^2. To quantitatively characterize the impact of irradiation on the hybridization of carbon atoms in different regions of a-C, the R3 model was selected for examination. We segmented the model into cubes with an

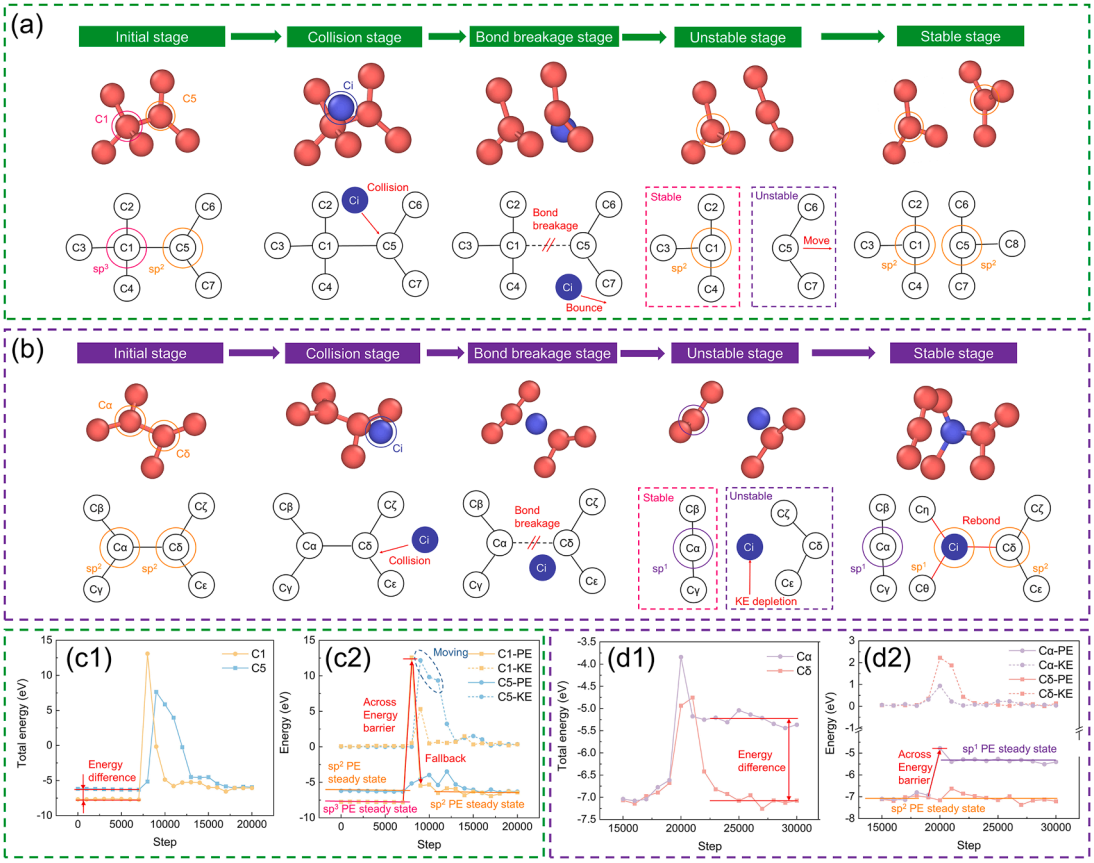

Fig. 6. Detailed microscopic diagram of hybridization evolution: (a) Atomic diagram of sp^3 to sp^2 transformation. The upper part is the atomic model diagram, and the lower part is a schematic diagram. C1–C8 represent the carbon atoms in the a-C matrix, and Ci represents the incident carbon atom; (b) Atomic diagram of sp^2 to sp^1 transformation, Cα–Cθ represent the carbon atoms in the a-C matrix; (c1) Total energy change in the sp^3-to-sp^2 transformation, taking atoms C1 and C5 as examples for comparison and explanation; (c2) Changes in potential energy and kinetic energy of atoms C1 and C5. PE stands for potential energy, KE stands for kinetic energy; (d1) Total energy change in the sp^2-to-sp^1 transformation; (c2) Changes in potential energy and kinetic energy of atoms Cα and Cδ. 10.000 time steps correspond to 1 ps.

edge length of 4 Å along the x, y, and z axes (Fig. 5(b1)). Subsequently, we evaluated the hybridization state within each segment to obtain a comprehensive, spatially resolved statistical analysis. Figs. 5(b2) and (b3) illustrate a notable hybridization change from sp^3 to sp^2 and sp^1 in the irradiated area, aligning well with experimental observations [11]. Additionally, owing to the cascading effect and heat generation induced by radiation, some transformation has also occurred in the periphery of the irradiation area. As a result of the irradiation-induced hybridization structure change, the sp^3 content in R3 model is lower than that in R0. Fig. 5(b4) proves that the relative content for each hybridization along the z direction is uniform throughout the core of the sample.

A detailed analysis of the hybridization transformation at the atomic scale is provided in Fig. 6. Fig. 6(a) illustrates the hybridization transition near the surface upon initial irradiation. Two differently hybridized carbon atoms (C1-sp^3, C5-sp^2) are connected by covalent bonds at first. Due to different hybridization states, there exists an energy difference between the two atoms (Fig. 6(c1)) [49]. The incident carbon atoms collide with C5, transferring approximately 12.5 eV of kinetic energy to C5. This results in the breaking of the bond between C1 and C5. This leads to a variation in the potential energy of C1, enabling it to surpass the energy barrier and undergo a transition from sp^3 to sp^2 hybridization (Fig. 6(c2)). Meanwhile, the C5 atom does not absorb enough energy to cross energy barriers, so that after experiencing a short period of energy fluctuation, it then moves to bond with the C8 atom, resulting in the formation of another stable sp^2 hybridization and exhibiting a final energy comparable with that of C1 (Fig. 6(c1)). Fig. 6(b) depicts the later stage of the cascade, where Cα and Cδ, initially both sp^2 hybridized carbon atoms connected by covalent bonds, have similar energies (Fig. 6 (d1)). The incident atom Ci collides with Cδ, expending nearly all of its kinetic energy, which results in the breaking of the covalent bond between Cα and Cδ. Cα absorbs sufficient energy to overcome the energy barrier for hybridization transition and subsequently transforms from sp^2 to sp^1 hybridization (Fig. 6(d2)). As the energy of the incident carbon atom is depleted, it remains in the matrix and bonds with Cδ, Cη, and Cθ, resulting in the formation of a sp^2 hybridization (Fig. 6(b)). Despite these structure and energy changes, after experiencing slight energy fluctuations, Cδ retains its sp^2 hybridization after the irradiation process (Fig. 6(d2)). It is worth mentioning that the difference in steady-state potential energy between sp^2 hybridized carbon in Fig. 6(c2) and (d2) is due to different environments. C1 and C5 are located near the surface with higher potential energy, while Cα and Cδ are located inside the matrix with lower potential energy.

4.2. *Nanoindentation simulations*

Fig. 7(a) shows the detailed parameters of the nanoindentation simulation, which is carried out within the irradiated area of a-C. The "loading force *vs.* time" curve shown in Fig. 7(b) for the nanoindentation simulations of the R0-R3 samples indicates that while the overall trend of the four curves is similar, there are notable differences in the slope of the loading section and the magnitude of the loading force during the holding section. This suggests that the mechanical properties of the samples undergo significant degradation as the irradiation dose increases. To quantitatively characterize the decline in elastic

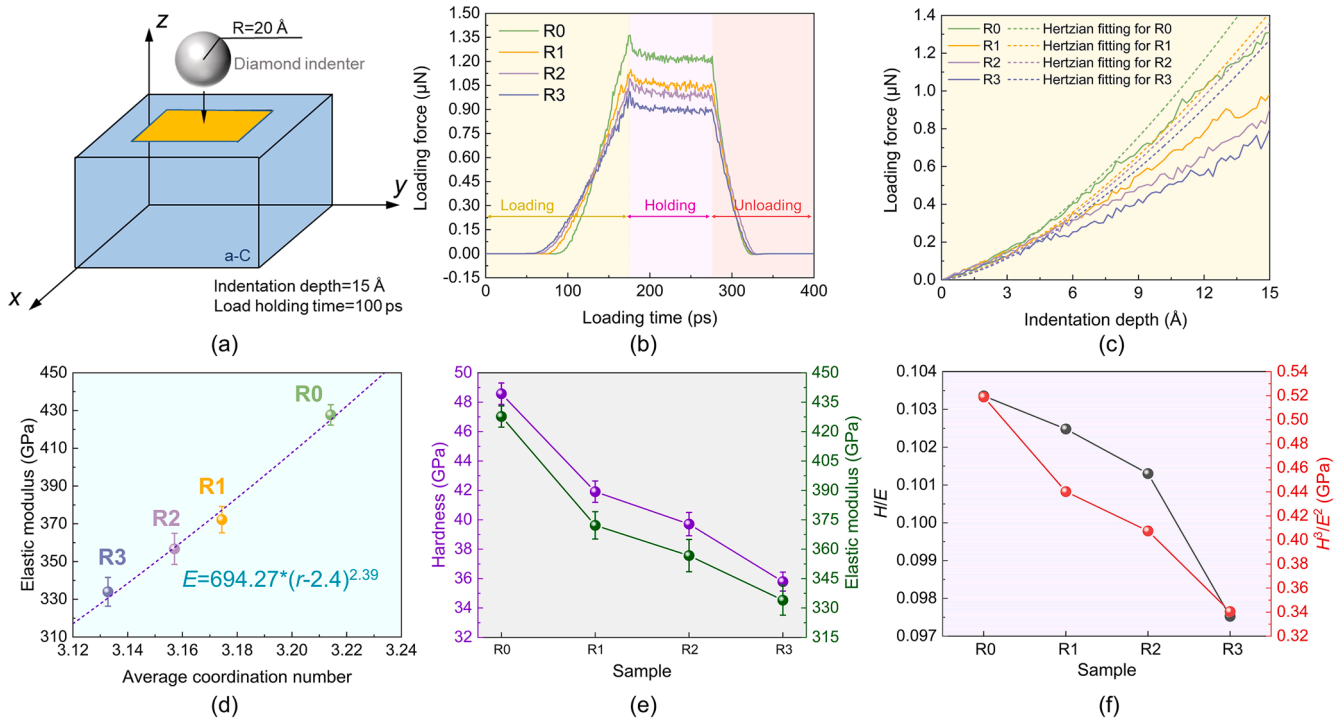

Fig. 7. Nanoindentation data statistics: (a) Sketch of the nanoindentation model, the yellow area represents the square where carbon atoms are randomly incident; (b) "Loading force *vs.* loading time" curves; (c) Hertzian fitting during the elastic stage of the loading; (d) "Elastic modulus *vs.* average coordination number" curve, showing a clear power exponent relationship; (e) Irradiation-affected decrease in hardness and elastic modulus of the 4 samples; (f) Changes in parameters (H/E, H^3/E^2) for qualitative prediction of material fracture toughness and wear resistance in the 4 samples. (For interpretation of the references to colour in this figure legend, the reader is referred to the web version of this article.)

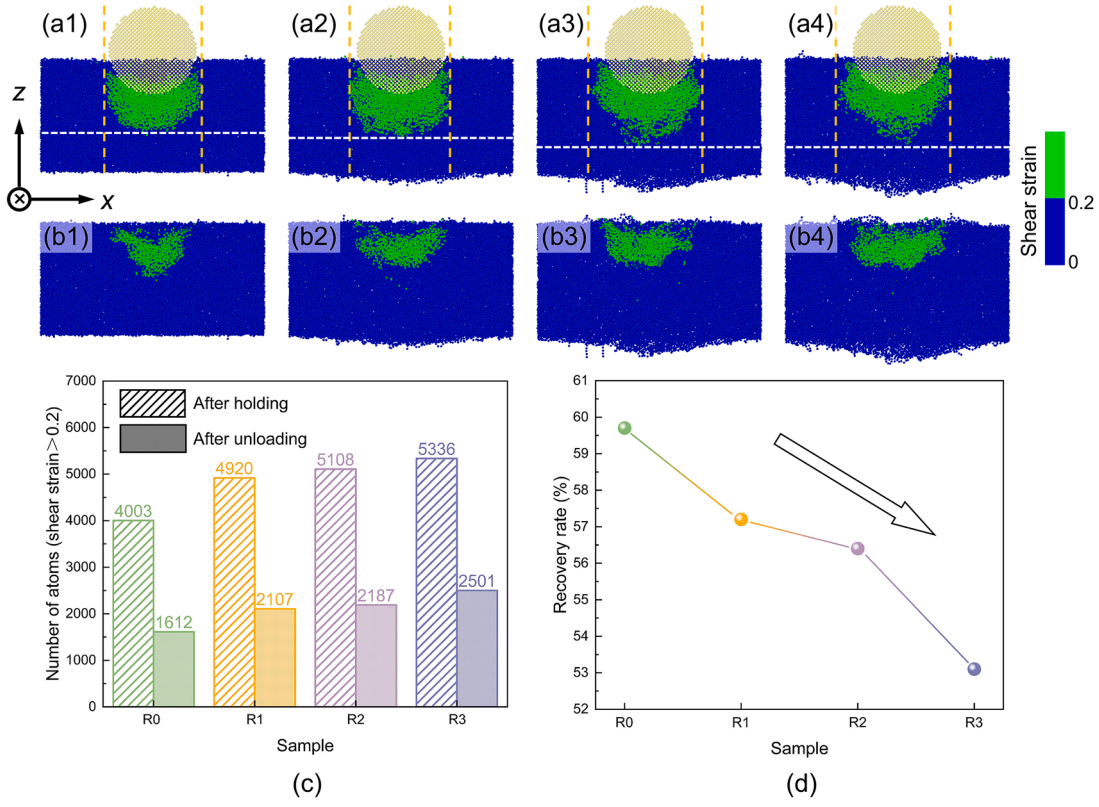

Fig. 8. Shear stain distribution of atoms (a) at the end of the holding stage and (b) at the end of the unloading stage during nanoindentation (1–4 correspond to R0-R3 models, respectively), the dashed yellow lines represent the extent of high-strain atoms along the x-direction, and the white line represents the maximum depth of high-strain atoms along the z-direction; (c) Statistical analysis of the number of atoms with shear strain > 0.2; (d) Recovery rate of the four samples after nanoindentation. (For interpretation of the references to colour in this figure legend, the reader is referred to the web version of this article.)

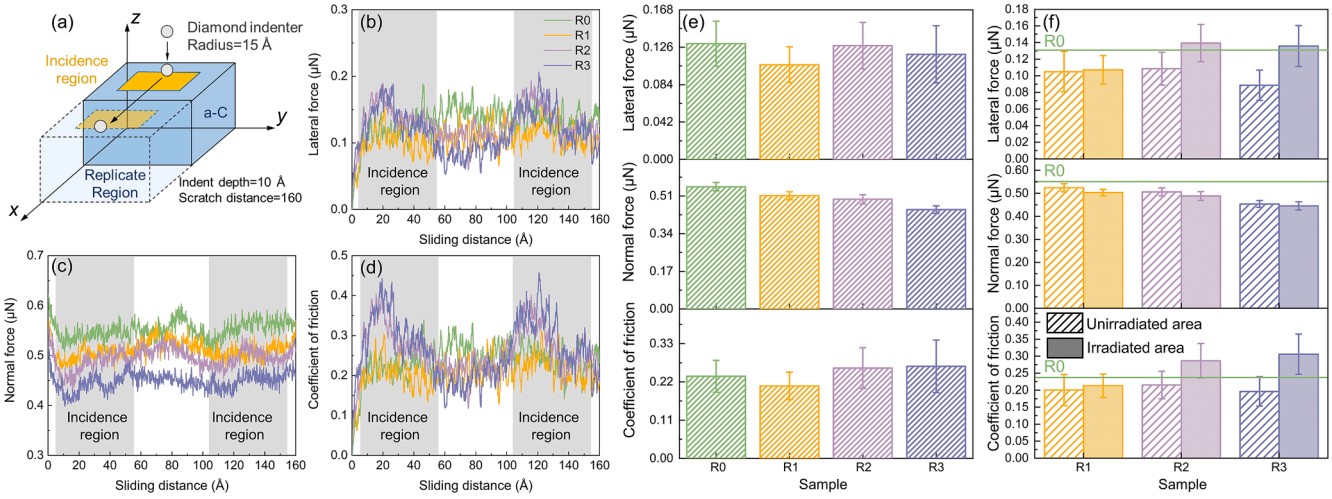

Fig. 9. Simulation of nanoscratch process: (a) Model schematic diagram; (b-d) Instantaneous lateral force, normal force, and CoF during the sliding process; (e) Average lateral force, normal force, and CoF; (f) Comparison between the irradiated and unirradiated areas of the four samples. The R0-R3 samples are represented by green, yellow, purple, and navy, respectively. (For interpretation of the references to colour in this figure legend, the reader is referred to the web version of this article.)

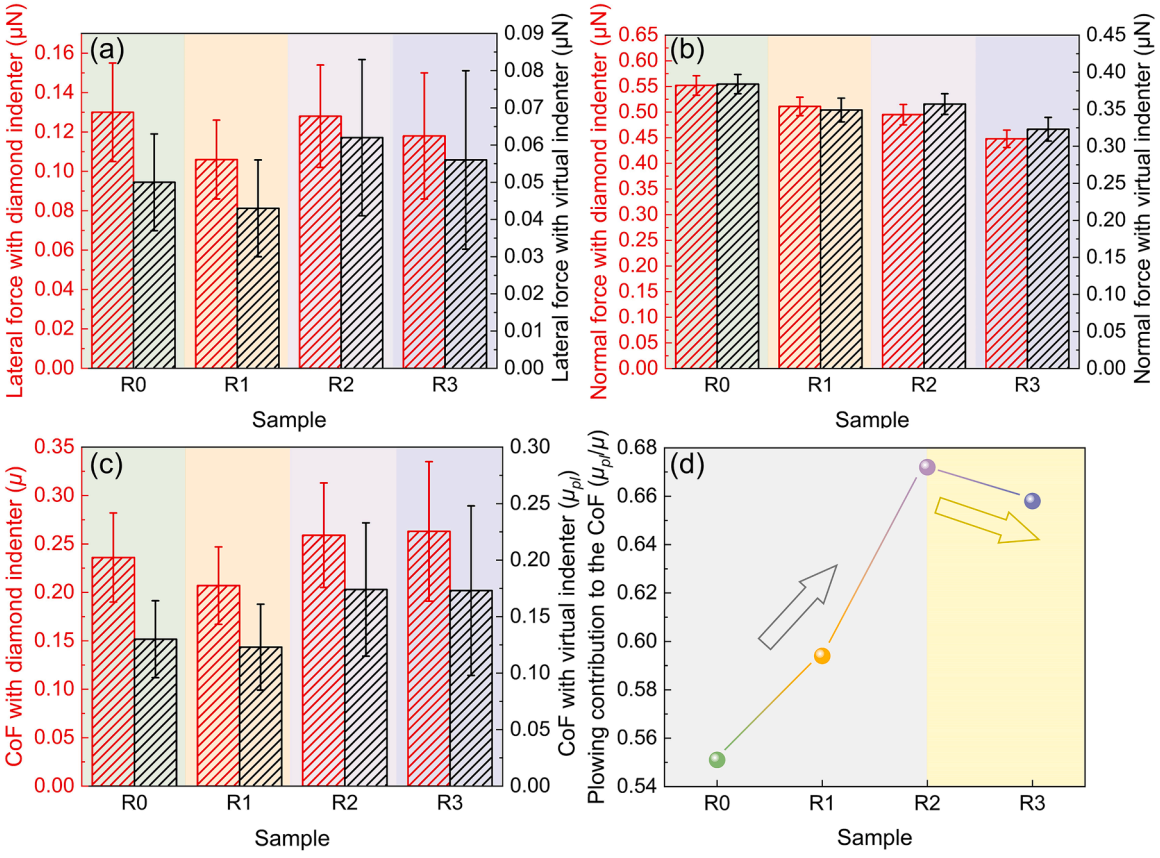

Fig. 10. Comparison between virtual indenter and diamond indenter for the 4 samples: (a) Averaged lateral force during the nanoscratch process; (b) Averaged normal force; (c) Averaged CoF; (d) Plowing contribution to the CoF calculated as μ_{pl}/μ.

performance, we apply the Hertz model, which is often used to describe the elastic deformation under contact loads to fit the elastic stage of loading [50,51]. The formula to calculate the loading force, as a function of the indentation depth, in Hertzian contact mechanics is given by [50]:

$$F = \frac{4}{3}E^*\sqrt{R}d^{\frac{3}{2}} \tag{6}$$

$$\frac{1}{E^*} = \frac{1-\nu_i^2}{E_i} + \frac{1-\nu_s^2}{E_s} \tag{7}$$

where E^* is the effective modulus derived from the properties of the indenter and the substrate, R is the radius of the indenter, and d is the depth of indentation. The effective modulus E^* is calculated using the Young's moduli and Poisson ratios of the indenter (E_i, ν_i) and the

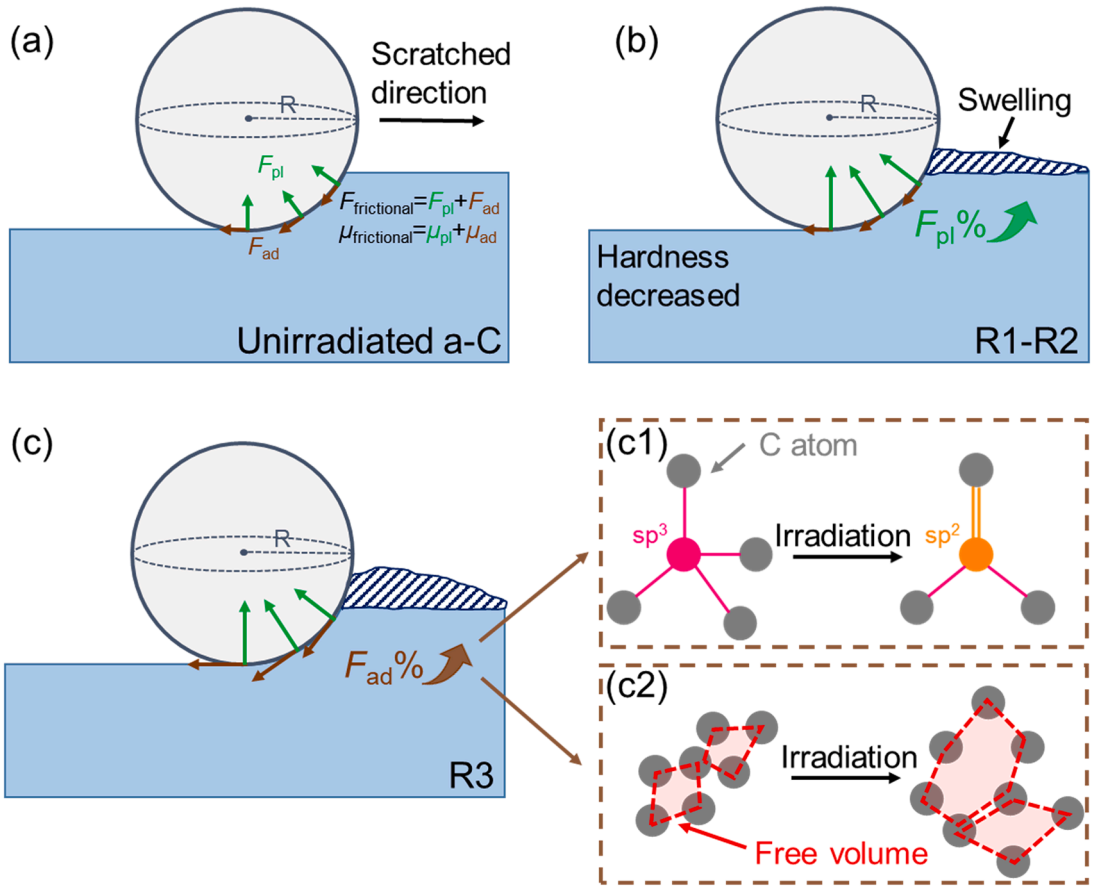

Fig. 11. Schematic diagram of the competition between adhesion and plowing during the scratch process: (a) Unirradiated samples, according to Bowden and Tabor's theory, F_{pl} and F_{ad} stand for plowing and adhesion components of frictional force, μ_{pl} and μ_{ad} stand for plowing and adhesion components of the CoF; (b) In the R1 and R2 models, the contribution of plowing to the CoF increases; (c) In the R3 model, the contribution of adhesion to the CoF increases, and (c1) and (c2) show the structure transformation responsible for the increase of adhesion.

substrate (E_s, ν_s). Since we assume the diamond indenter to be a rigid body and neglect its internal forces, Eq. (7) can be written as:

$$E_s = E^*\left(1-\nu_s^2\right) \tag{8}$$

According to Fig. 7(c), the calculated E_s of R0 is around 430 GPa. This outcome is similar to the experimental value of a-C with the same density (~450 GPa [1,52]). This similarity underscores the reliability and validity of the present simulation [53]. We continue to calculate the elastic modulus of R1-R3 and fit them in the power-law relationship proposed by He et al. [54], which is described as follows:

$$E = k(r-2.4)^m \tag{9}$$

where E is the elastic modulus, r is the average coordination number, k and m are the fitting parameters. The result of fitting Eq. (9) to our data yields $k = 694.27$ and $m = 2.39$, illustrating that it conforms to an exponential relationship (Fig. 7(d)). The modulus of the irradiated sample decreases noticeably as the irradiation dose increases, correlating with a reduction in sp^3 content. Within a-C, sp^3 hybridized carbon often serves as a structural skeleton providing support, whereas sp^2 hybridized carbon forms short-chain clusters that act as fillers. As a result, the decreased sp^3/sp^2 ratio leads to a significant decrease in the material's resistance to deformation. Moreover, irradiation leads to an increase in the free volume of the sample (Fig. 4(d)), consequently resulting in a reduction of its modulus. We computed the hardness using the approach outlined by Valencia et al. [53], revealing that the R0-R3 models exhibited a trend akin to the elastic modulus (Fig. 7(e)), *i.e.*, the value decreases with increasing irradiation dose. The material's resistance to wear can be empirically described by the values of H/E and H^3/E^2, with higher values indicating better wear resistance [55]. We calculated the values for three samples and observed a decrease due to irradiation (Fig. 7(f)), consistent with the subsequent discussion on the deterioration of wear resistance performance.

Fig. 8(a) and (b) illustrate the atomic shear stain during loading and unloading phases of the R0-R3 samples, respectively. In amorphous materials, atoms with a shear strain larger than 0.2 are frequently employed to characterize local plastic deformation within the substrate [56]. During the loading phase, the plastic region in R0 samples is narrow and shallow. As the irradiation dose increases, the deformation zone gradually expands, evidenced by the width of the zone marked by the yellow dashed lines growing larger and the deformation zone becoming deeper (white dashed line). The transition from sp^3 to sp^2 bonds increases the flexibility of the a-C, which is responsible for the larger deformation zone after irradiation damage. The sp^2 hybridized structure tends to buckle and deform more readily than the sp^3 hybridized structure, facilitating the material's ability to disperse stress across a broader area when subjected to stress. Moreover, the increase in free volume causes a transition from solid-like to liquid-like behavior within the sample, allowing strain to be transmitted over a wider range with an increased number of atoms experiencing high strain (Fig. 8 (c)). We also calculated the elastic recovery after unloading and observed that the rebound becomes increasingly difficult with higher irradiation doses (Fig. 8(d)). In Fig. 8(a) and (b), no significant shear bands are observed away from the indenter, which contrasts with amorphous metallic materials [53,57].

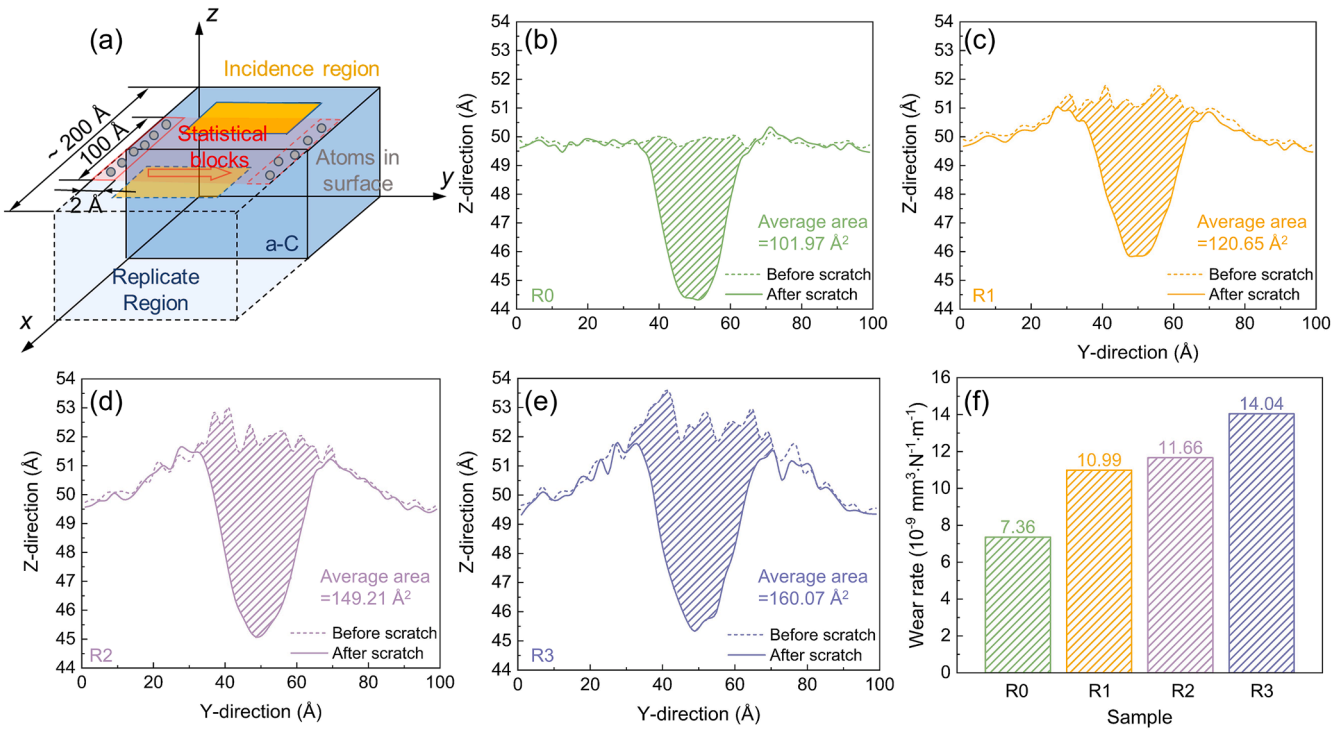

Fig. 12. Statistics results of the wear rate: (a) Schematic diagram for obtaining the cross-sectional profile; (b-e) cross-sectional wear profile of the R0-R3 samples; (f) Wear rate comparison of the four samples.

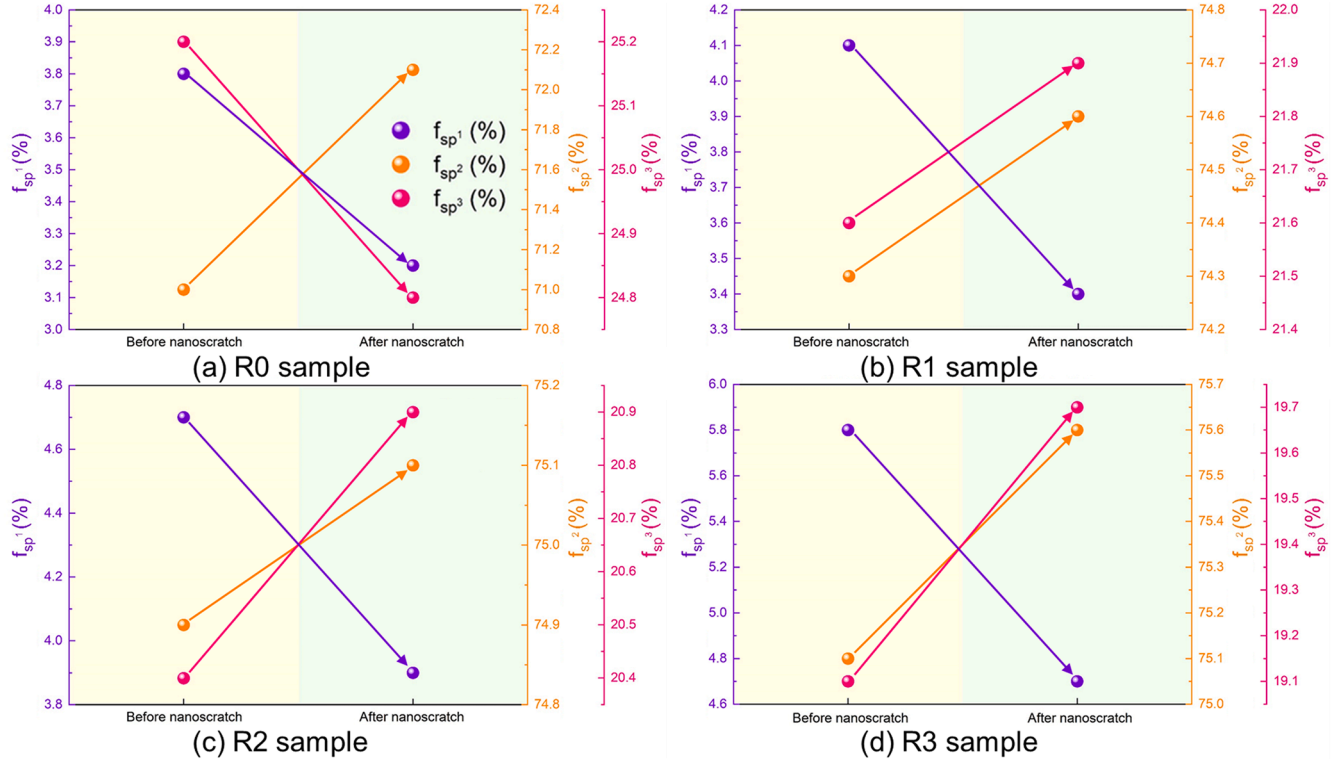

Fig. 13. Statistical analysis of carbon atom hybridization transformation in the four samples after the scratching process: (a)-(d) represent the R0-R3 samples. The content of sp^1, sp^2 and sp^3 are represented by purple, orange and pink, respectively. (For interpretation of the references to colour in this figure legend, the reader is referred to the web version of this article.)

4.3. Nanoscratch simulations

After replicating the system once along the x-axis, we performed displacement-controlled nanoscratch simulations on the R0-R3 samples. The results are presented in Fig. 9. We analyzed the evolution of lateral force, normal force, and the coefficient of friction (CoF, defined as

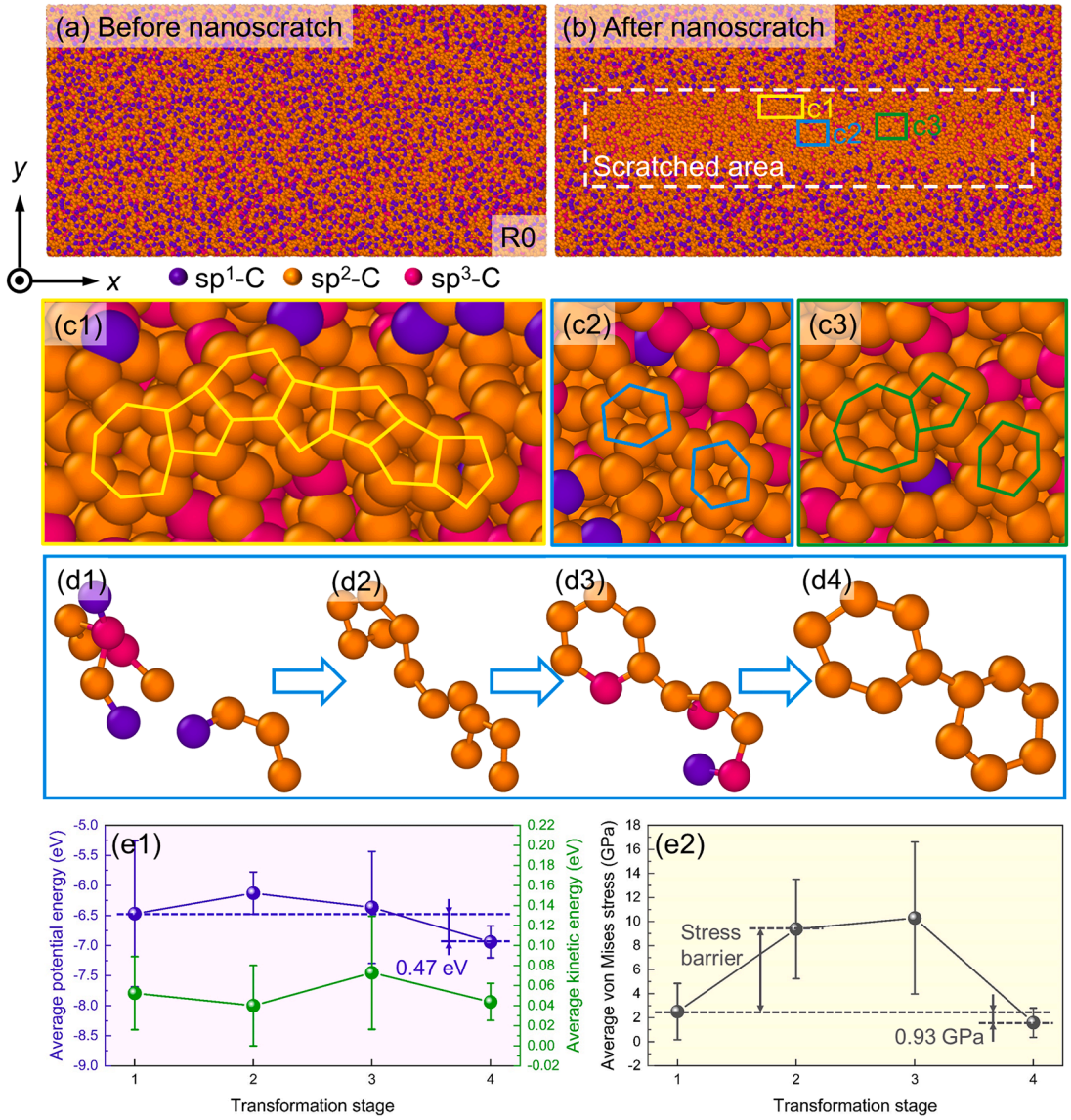

Fig. 14. Nanoscratch analysis of the R0 model: (a-b) Top view of the overall morphology before and after scratching; (c) Graphene-like structure at the bottom of the scratched region, shown as the local magnification of the boxed area in (b); (d) Detail of atomic evolution of (c2); (e1) Potential energy and kinetic energy change during hybridization transformation process of (d); (e2) Von Mises stress changes during the hybridization transformation process of (d).

lateral force divided by normal force [58]) during the sliding process, as shown in Fig. 9(b)–(d). Regarding the averaged lateral force, the irradiated samples exhibited a reduction compared to the unirradiated ones. This decrease is attributed to the lubricating effect of sp^2 carbon induced by irradiation. The CoF in the irradiated region, however, is higher than that in the unirradiated region due to surface swelling caused by irradiation, which hinders the movement of the indenter. (Fig. 9(f) top). The magnitude of the averaged normal force in the four models notably decreases as the irradiation dose increases (Fig. 9(e) middle), and it is lower in the irradiation area than in the unirradiated area (Fig. 9(f) middle) due to the reduced hardness, as mentioned in Section 3.2. On the other hand, the irradiation led to a rise in the average CoF for the R2 and R3 samples (Fig. 9(e) bottom), whereas the R1 sample exhibits a CoF lower than the original R0 sample.

Bowden and Tabor proposed that friction primarily originates from two aspects: adhesion between contacting solid surfaces and plastic plowing deformation of the substrate. Therefore, the CoF (μ) can be described as the sum of contributions of both plowing (μ_{pl}) and adhesion (μ_{ad}) components:$\mu = \mu_{pl} + \mu_{ad}$.To quantitatively elucidate the impact of these two factors on a-C after irradiation, a virtual, purely repulsive indenter with a force constant of 10 eV/Å^3 is introduced to compare the resulting nanoscratch processes with the ones conducted with the explicit indenter. This approach allows the exclusion of the contribution of adhesion to friction, focusing solely on the effects of plowing deformation, and μ_{pl} is calculated by dividing the averaged lateral force during the scratch process of the virtual indenter by the averaged normal force. According to Fig. 10(a)–(c), after switching to the virtual indenter, due to the absence of the adhesion term, both lateral and normal forces are reduced by varying degrees, and CoF also decreases. The contribution of plowing to CoF (μ_{pl}%) is defined by: $\mu_{pl}\% = \mu_{pl}/\mu$, which is calculated to be between 1/2 and 2/3. This ratio first increases and then decreases with the increase in the irradiation dose (Fig. 10(d)), with the trend being more significant at higher doses (Fig. S2), indicating a competitive mechanism between adhesion and plowing as shown in Fig. 11. When the irradiation dose is low (R0-R2) and the irradiation dose is increasing, the increased plowing contribution to friction (as a parameter sensitive to the penetration depth of the indenter [59]) might be due to surface swelling (Fig. 11(b)). On the other hand, as the irradiation dose increases, the transformation of sp^3 to sp^2 structure (Fig. 11(c1)) and increase in free volume (Fig. 11(c2)) lead to a change from a

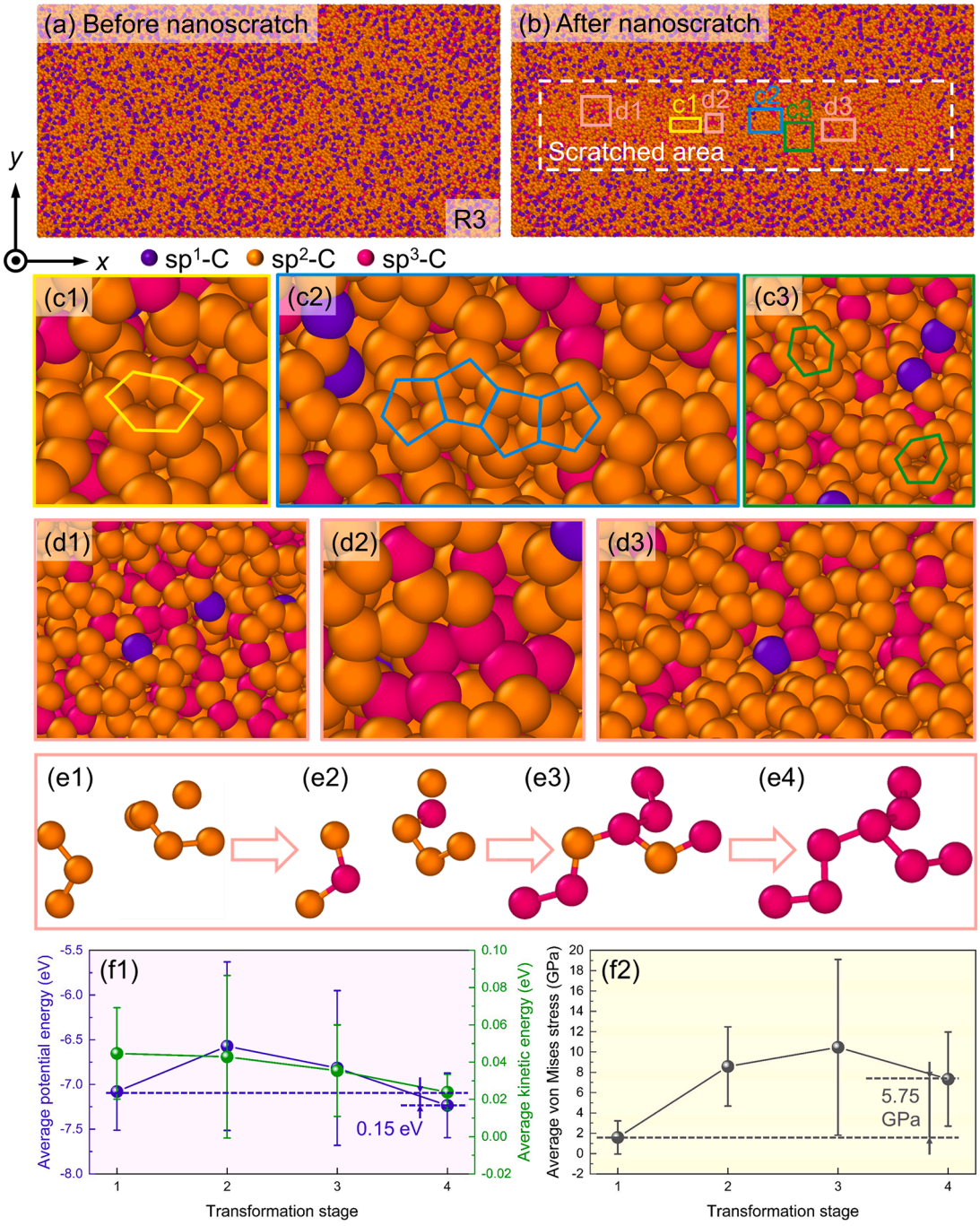

Fig. 15. Nanoscratch analysis of the R3 model: (a-b) Top view of the overall morphology before and after scratching; (c) The enlarged graphene-like structure at the bottom of the scratched region, selected in the yellow, blue and green boxed area marked in (b); (d) The typically enlarged aggregated sp^3 hybridized carbon atoms, selected in the pink boxed area in (b); (e) Detail of atomic evolution of the region shown in (d2); (f1) Potential energy and kinetic energy change during the hybridization transformation process of (e); (f2) Von Mises stress changes during the hybridization transformation process of (e). (For interpretation of the references to colour in this figure legend, the reader is referred to the web version of this article.)

commonly said "solid-like" to a "liquid-like" state within the amorphous material. This change facilitates the contacting force between the indenter and a-C [60], thereby promoting adhesion and weakening the relative contribution of plowing to the overall CoF.

We calculated the wear rate of the four samples after the nanoscratch process. The statistical approach involved extracting the atomic coordinates on the surface and calculating the average z-position along the x-direction, as schematically shown in Fig. 12(a). The cross-sectional wear area is determined by calculating the difference in surface profile before and after the scratch (Fig. 12(b)–(e)). The wear rate is then calculated using the formula [61]:

$$\omega = \frac{S}{F} \tag{10}$$

where ω is the wear rate, S is the averaged wear cross-sectional area, and F is the averaged normal force. We found that the wear rate increases with the irradiation dose, with the wear rate of the R3 sample being nearly twice that of the R0 sample (Fig. 12(f)). This significant increase in wear rate can primarily be attributed to changes in hybridization and an increase in free volume. The transition from sp^3 to sp^2 bonding, as a

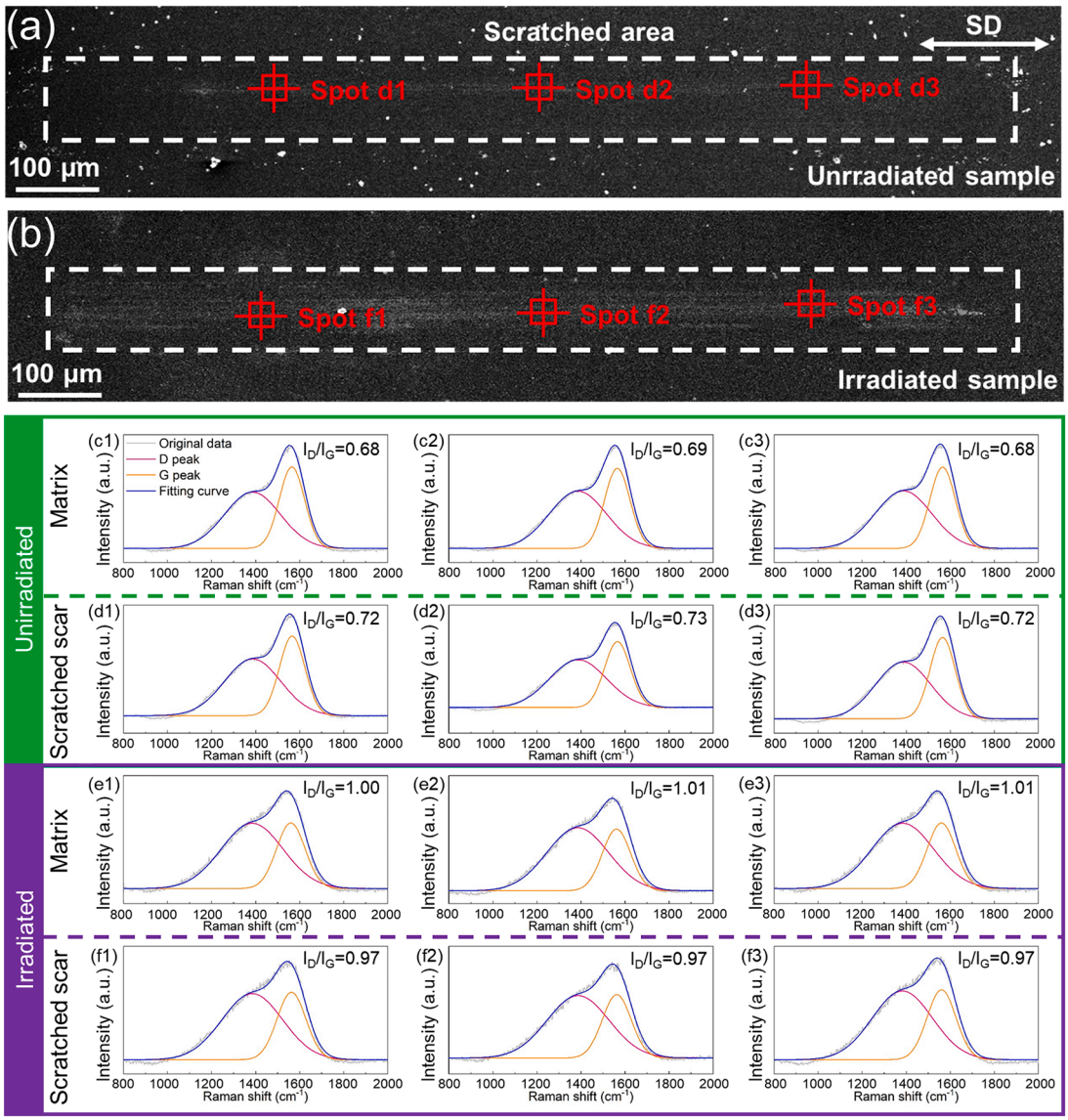

Fig. 16. Scratch morphology and Raman spectroscopy characterization: (a-b) SEM images showing the scratch morphology (SD is the sliding direction); (c-d) Raman spectroscopy of the unirradiated sample. (c1-c3) are taken from different positions on the matrix film (not marked in the figure) and (d1-d3) are taken from different positions in the scratched region; (e-f) Raman spectroscopy of the irradiated sample (matrix and scratched scar).

result of irradiation, deteriorates the material's resistance to wear by making it more susceptible to material removal processes during sliding.

As a metastable material, a-C is also found to undergo hybridization transformation during nanoscratching as illustrated in Fig. 13. The sp^1-hybridized carbon content in all four samples decreased after scratching, due to compressive-stress-assisted rebonding of carbon atoms on the surface, which is consistent with previous observations [21]. Intriguingly, all three irradiated samples demonstrated an unusual rise in sp^3 content after scratching (Fig. 13(b)–(d)), contrasting with the decrease trend observed in unirradiated samples (Fig. 13(a)). Some additional constant- load nanoscratch simulations also featured this abnormal phenomenon (Figs. S3 and S4).

The above hybridization transformation is further elucidated through atomic-scale observation, as shown in Fig. 14 for the R0 sample. The sp^1 carbon content decreases distinctly on the scratched area (Fig. 14(a) and (b)). Furthermore, the presence of a graphene-like multicomponent ring observed in the wear tracks (Fig. 14(c)) provides a compelling explanation for the reduction in frictional force in a-C. This observation supports the claim that mechanical wear in a-C can induce the formation of more thermodynamically stable, graphitic (sp^2 hybridized) structures [62-64]. The atomic evolution process for graphene-like rings in Fig. 14(c2) are given in Fig. 14(d), showing the connection of carbon chains and gradual transformation towards two sp^2 six-membered rings. The kinetic energy, as shown in Fig. 14(e1), exhibits minimal variation, thereby ruling out any significant temperature influence on this transformation. The maximum temperature during sliding is less than 500 K, far from reaching the transformation temperature (<1000 K) of sp^3 to sp^2 hybridization [65]. The averaged potential energy of per-atom has decreased by 0.47 eV, indicating that the transition process is toward a thermodynamically stable state. Fig. 14 (e2) displays the stress evolution throughout the four stages, exhibiting the presence of a stress barrier during the transformation process. Similar to the trend of the potential energy changes, the stress in stage 4 is lower than that in the initial stage, indicating that the transition is moving towards structural stability.

In the case of the R3 model, a reduction in sp^1 carbon atoms on the surface is also observed after scratching (Fig. 15(a) and (b)), accompanied by the formation of a graphene-like structure within the wear scar (Fig. 15(c)), similar to that shown in Fig. 14(c). Anomalously, we found that the gathered sp^3 skeleton structure like Fig. 15(d) at the bottom of

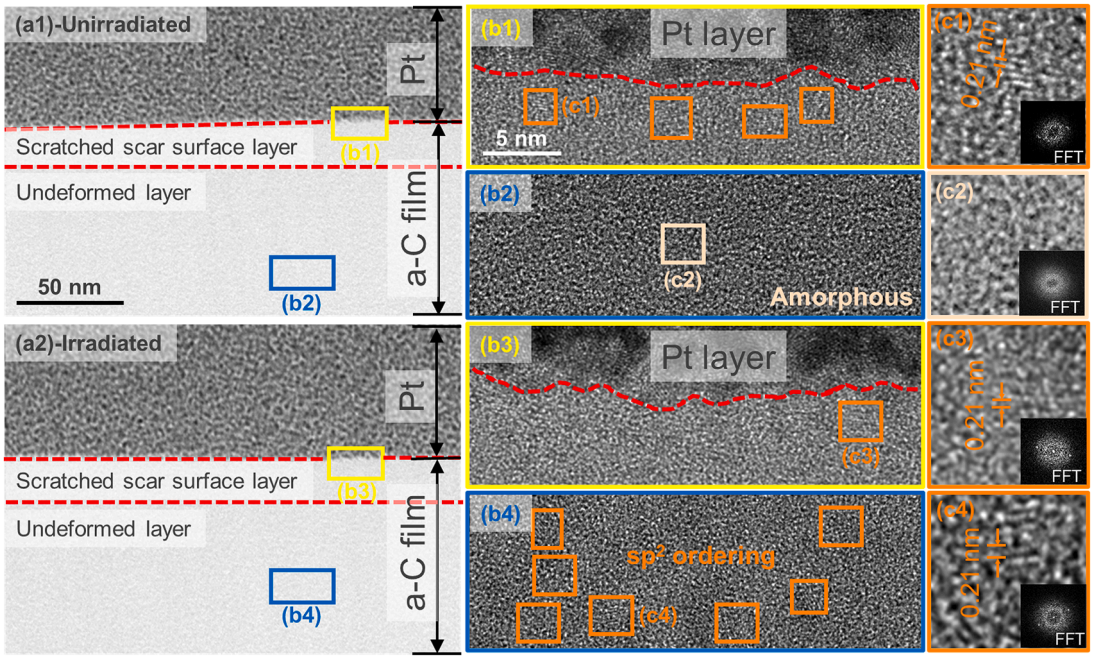

Fig. 17. Analysis of TEM images of unirradiated and irradiated samples: (a1), (a2) Cross-sectional bright-field images of the scratched scar of unirradiated and irradiated samples; (b1), (b2) High-resolution TEM images of the scratched surface layer and the undeformed layer of the unirradiated sample, with the yellow box showing the local sp^2 nanostructures; (b3), (b4) High-resolution TEM images of the scratched surface layer and the undeformed layer of the irradiated sample; (c1) - (c4): Enlarged microstructures and Fast Fourier Transforms (FFT) of each selected area in (b1) - (b4). The scale bar in (a) is 50 nm, and the scale bar in (b) is 5 nm. (For interpretation of the references to colour in this figure legend, the reader is referred to the web version of this article.)

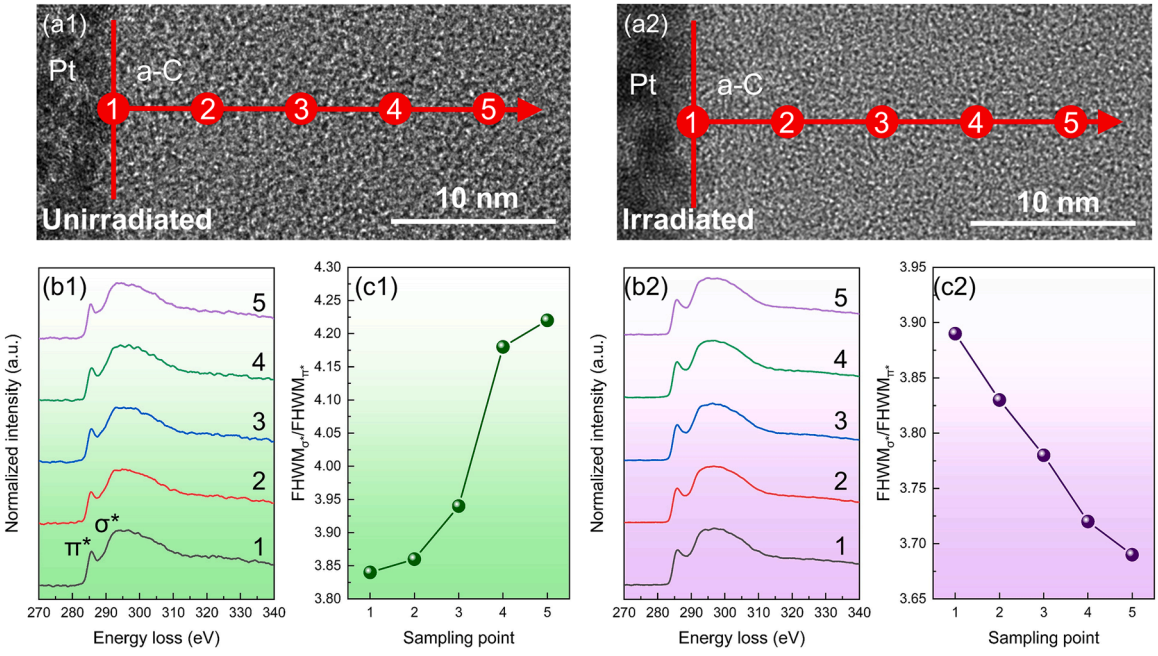

Fig. 18. EELS characterization of the scratched scar surface layer: (a1), (a2) HRTEM image of the unirradiated and irradiated a-C film, the number represents the location of the sampling point for EELS data collection; (b1), (b2) EELS spectrum of five sampling points for unirradiated and irradiated samples; (c1), (c2) The full width at half maximum (FWHM) ratio of σ* peak to π* peak in two samples.

the scratched scar. From the perspective of data statistics, it manifests as the increased sp^3 content in the R3 sample as illustrated in Fig. 13(d). The evolution process of atoms depicted in Fig. 15(d2) was monitored, wherein the dispersed sp^2 carbon atoms underwent aggregation and eventually merged to form the sp^3 cluster, as illustrated in Fig. 15(e). Likewise, we investigated the changes in energy and stress during this process and discovered that the transformation was also driven by stress rather than temperature. The overall potential energy decreased slightly (Fig. 14(e1)), but this is a natural result because according to Fig. 6(c2), the potential energy of sp^3 is lower than that of sp^2. Notably, a significant amount of stress remains within the sp^3 atoms (Fig. 15(f2)) which is different from Fig. 14(e2), suggesting the meta-stable nature of this transformation. This stress-induced sp^2 to sp^3 transformation has been reported in graphite [66] and certain a-C with low sp^3 content [29].

Moreover, defects within the a-C, such as dangling bonds or pores, serve as nucleation points that facilitate the transition from sp^2 to sp^3 hybridization. These imperfections offer favorable conditions for the reorganization of carbon atoms, leading to the formation of sp^3 bonds.

4.4. Experimental validation

To demonstrate the reliability of our simulations, we performed scratch experiments on unirradiated and irradiated samples as shown in Fig. 16(a) and (b). We observed that the scratches on the irradiated samples were more obvious than that on the unirradiated sample under the same loading conditions, suggesting reduced wear resistance after irradiation (Fig. 12). Raman spectroscopy serves as an efficient, non-destructive technique for analyzing the intricate bonding configurations within a-C films. The spectral data of matrix and scratched scar are presented in Fig. 16(c)–(f). As indicated, the peak spanning 800–2000 cm^{-1} was analyzed by Gaussian fitting, allowing for the identification of the D (disorder) peak in the vicinity of 1380 cm^{-1} and the G (graphitic) peak around 1560 cm^{-1}. Generally, a higher intensity ratio of the D peak to the G peak (I_D/I_G) indicates a lower proportion of sp^3 hybridization [2]. After conducting three repeated tests at different spots (Spots d1-d3 and f1-f3 shown in Fig. 16(a) and (b), the spots in the matrix are not shown in due to the small scale), we noted that in the unirradiated samples, the I_D/I_G ratio increased after scratching, indicating a reduction in sp^3 content; whereas in the irradiated samples, it decreased, which also aligns well with our simulation results. Comparing Fig. 16(c) and (e), the reason for the increase in I_D/I_G is due to the large number of defective carbon atoms generated by irradiation, leading to an increase in the disordered structure [67].

To further validate the rationality of this transformation, we conducted TEM analysis of the scratched structure beneath the wear scars. The cross-sectional bright-field images of the wear scar are shown in Fig. 17(a), and selected high-resolution TEM observations of the scratched surface and the undeformed substrate layer are shown in Fig. 17b. For the unirradiated a-C film, the substrate exhibits a typical disordered amorphous structure (Fig. 17(b2) and (c2)). However, after scratching, layered sp^2 ordering appears in the scratched surface layer, with an interlayer spacing of 0.21 nm, which is estimated to be the (100) plane of graphite [68]. The irradiated a-C film exhibits a significantly higher degree of sp^2 ordering structures within the undeformed layer, in comparison to the original fully amorphous structure shown in Fig. 17 (b2). The direct experimental evidence presented here confirms the irradiation-induced transformation of carbon atoms from sp^3 to sp^2 hybridization. Meanwhile, the layered sp^2 ordering in the scratched scar surface layer is less than in the undeformed layer, which proves a decrease in sp^2-hybridized carbon content in the scratch scar and correlates well with the previous Raman and simulation results.

Electron energy loss spectroscopy (EELS) is an important method for analyzing the hybridization level of carbon atoms. A larger intensity difference between the σ* and π* peaks suggests a higher sp^3/sp^2 ratio [68-70]. We selected 5 points at equal intervals from the center to the border of the scratched scar surface layer for analysis in both unirradiated and irradiated samples (Fig. 18(a1) and (a2)). By deconvolution of the two peaks shown in Fig. 18(b1) and (b2), we obtained the scale of Fig. 18(c1) and (c2). In the unirradiated sample, there was an increase in the ratio of $FWHM_{\sigma^*}/FWHM_{\pi^*}$ (FWHM: full width at half maximum) from the surface to the maximum scratch depth, indicating that scratching reduces the sp^3 content in the surface (Fig. 18(c1)). Nevertheless, in the irradiated sample, the closer the sampling point is to the surface, the higher $FWHM_{\sigma^*}/FWHM_{\pi^*}$ ratio (Fig. 18(c2)), which supports the previously mentioned abnormal transformation from sp^2 hybridization to sp^3 hybridization.

5. Conclusions

This molecular dynamics study provides a thorough investigation into the structural, mechanical, and hybridization changes in amorphous carbon (a-C) caused by irradiation. By combining advanced simulation techniques with detailed experimental analytical methods, the research offers significant contributions to the understanding of a-C behavior under irradiation. We draw the following conclusions:

(1) Irradiation can cause the surface of a-C to bulge, introducing compressive stresses that cause changes in bond angle and bond length, weakening the optimal distribution of Voronoi polyhedra of a-C and exacerbating amorphization. The increase in sp^2 content is the main transformation mechanism of hybridization, and this transformation process was analyzed from the perspective of atomic configuration.
(2) Nanoindentation reveals that irradiation weakens the a-C in terms of hardness and elastic modulus, which is related to hybridization transformation and an increase in free volume.
(3) The coefficient of friction of a diamond indenter against the a-C increases with the irradiation dose, mainly due to a decrease in the normal force, and the wear rate increases as well. Nanoscratching can cause a-C to form graphene-like structures, and the irradiated samples undergo a metastable hybridization transition featuring an increase in sp^3 content, which we confirmed by Raman spectroscopy and TEM-EELS.

CRediT authorship contribution statement

Yeran Shi: Writing – original draft, Validation, Software, Methodology, Investigation, Formal analysis, Data curation. **Qiaosheng Xia:** Investigation, Data curation. **Mingda Xie:** Investigation, Data curation. **Qing Zhou:** Writing – review & editing, Funding acquisition, Conceptualization. **Dongpeng Hua:** Investigation, Data curation. **Liqiang Chai:** Writing – review & editing, Data curation. **Tan Shi:** Writing – review & editing. **Stefan J. Eder:** Writing – review & editing, Data curation. **Haifeng Wang:** Writing – review & editing, Supervision, Funding acquisition. **Peng Wang:** Data curation. **Weimin Liu:** Writing – review & editing.

Declaration of competing interest

The authors declare that they have no known competing financial interests or personal relationships that could have appeared to influence the work reported in this paper.

Acknowledgments

The authors would like to thank the National Key Research and Development Program of China (2022YFB3809000), Natural Science Foundation of China (52175188), Key Research and Development Program of Shaanxi Province (2023-YBGY-434), Science and Technology on Reactor System Design Technology Laboratory. SJE acknowledges Project K2 InTribology2, no. 906860 of the Austrian Research Promotion Agency (FFG). Open access funding was provided by TU Wien.

Supplementary materials

Supplementary material associated with this article can be found, in the online version, at doi:10.1016/j.actamat.2024.120424.

References

[1] J. Robertson, Diamond-like amorphous carbon, Mater. Sci. Eng.: R: Rep. 37 (4) (2002) 129–281.
[2] A.C. Ferrari, J. Robertson, Interpretation of Raman spectra of disordered and amorphous carbon, Phys. Rev. B 61 (20) (2000) 14095–14107.
[3] J. Robertson, Mechanical-properties and structure of diamond-like carbon, Diam. Relat. Mater. 1 (5–6) (1992) 397–406.

[4] J.H. Sui, W. Cai, Mechanical properties and anti-corrosion behavior of the diamond-like carbon films, Surf. Coat. Technol. 201 (3–4) (2006) 1323–1327.
[5] M. Aggleton, J.C. Burton, P. Taborek, Cryogenic vacuum tribology of diamond and diamond-like carbon films, J. Appl. Phys. 106 (1) (2009).
[6] A.A. Voevodin, J.S. Zabinski, Nanocomposite and nanostructured tribological materials for space applications, Compos. Sci. Technol. 65 (5) (2005) 741–748.
[7] B. Shi, Y.X. Wu, Y. Liu, L.M. Wang, J. Gao, H.J. Hei, K. Zheng, S.W. Yu, A review on diamond-like carbon-based films for space tribology, Mater. Sci. Technol. 38 (15) (2022) 1151–1167.
[8] X.Q. Fan, Q.J. Xue, L.P. Wang, Carbon-based solid-liquid lubricating coatings for space applications-a review, Friction 3 (3) (2015) 191–207.
[9] S. Porro, G. De Temmerman, S. Lisgo, D.L. Rudakov, A. Litnovsky, P. Petersson, P. John, J.I.B. Wilson, Diamond coatings exposure to fusion-relevant plasma conditions, J. Nucl. Mater. 415 (1) (2011) S161–S164.
[10] S.V. Hainsworth, N.J. Uhure, Diamond like carbon coatings for tribology: production techniques, characterisation methods and applications, Int. Mater. Rev. 52 (3) (2007) 153–174.
[11] Q. Zhou, Z. Jiao, Z. Huang, Y. Shi, Y. Li, C. Yin, H. Wang, H. Pinto, C. Greiner, W. Liu, Wear-resistant CrCoNi nanocrystalline film via friction-driven surface segregation, Acta Mater. 279 (2024) 120299.
[12] Y. Shen, Z. Zhang, B. Liao, X. Wu, X. Zhang, Comparative study on effects of Ni ion implantation on amorphous carbon (a-C) coating and tetrahedral amorphous carbon (ta-C) coating, Nucl. Instrum. Method. Phys. Res. Sect. B: Beam Interact. Mater. Atom. 467 (2020) 1–8.
[13] Q. Zhou, D. Luo, D. Hua, W. Ye, S. Li, Q. Zou, Z. Chen, H. Wang, Design and characterization of metallic glass/graphene multilayer with excellent nanowear properties, Friction 10 (11) (2022) 1913–1926.
[14] D. Hua, Q. Zhou, Y. Shi, S. Li, K. Hua, H. Wang, S. Li, W. Liu, Revealing the deformation mechanisms of <110>symmetric tilt grain boundaries in CoCrNi medium-entropy alloy, Int. J. Plast. (2023) 103832.
[15] Y. Ren, Q. Zhou, D. Hua, Z. Huang, Y. Li, Q. Jia, P. Gumbsch, C. Greiner, H. Wang, W. Liu, Wear-resistant CoCrNi multi-principal element alloy at cryogenic temperature, Sci. Bull. 69 (2) (2024) 227–236.
[16] Y. Shi, W. Ye, D. Hua, Q. Zhou, Z. Huang, Y. Liu, S. Li, T. Guo, Y. Chen, S.J. Eder, H. Wang, Interfacial engineering for enhanced mechanical performance: high-entropy alloy/graphene nanocomposites, Mater. Today Phys. 38 (2023) 101220.
[17] H. Chen, G. Zhang, Z. Lu, L. Bai, Frictional behaviors of diamond-like carbon films under water lubrication: a molecular dynamics study, Tribol. Int. 153 (2021) 106609.
[18] E.J. Sandoz-Rosado, O.A. Tertuliano, E.J. Terrell, An atomistic study of the abrasive wear and failure of graphene sheets when used as a solid lubricant and a comparison to diamond-like-carbon coatings, Carbon N.Y. 50 (11) (2012) 4078–4084.
[19] Y. Wang, N. Yamada, J. Xu, J. Zhang, Q. Chen, Y. Ootani, Y. Higuchi, N. Ozawa, M.-I.D.B. Bouchet, J.M. Martin, S. Mori, K. Adachi, M. Kubo, Triboemission of hydrocarbon molecules from diamond-like carbon friction interface induces atomic-scale wear, Sci. Adv. 5 (11) (2019) eaax9301.
[20] L. Wang, Z. Zhang, H. Chen, H. Wang, Y. Liu, J. Wang, M. Wang, Friction behavior of diamond-like carbon coatings with different sp3 contents by atomistic-scale friction dynamics, Surf. Coat. Technol. 464 (2023) 129580.
[21] X. Li, A. Wang, K.-R. Lee, Insights on low-friction mechanism of amorphous carbon films from reactive molecular dynamics study, Tribol. Int. 131 (2019) 567–578.
[22] W. Ren, F. Djurabekova, K. Nordlund, Swift heavy ion effects on DLC-nanotube-diamond thin films, J. Phys. D Appl. Phys. 50 (35) (2017) 355301.
[23] J. Liu, H. Vázquez Muíños, K. Nordlund, F. Djurabekova, Molecular dynamics simulation of the effects of swift heavy ion irradiation on multilayer graphene and diamond-like carbon, Appl. Surf. Sci. 527 (2020) 146495.
[24] L. Martínez, R. Andrade, E.G. Birgin, J.M. Martínez, PACKMOL: a package for building initial configurations for molecular dynamics simulations, J. Comput. Chem. 30 (13) (2009) 2157–2164.
[25] A.P. Thompson, H.M. Aktulga, R. Berger, D.S. Bolintineanu, W.M. Brown, P. S. Crozier, P.J. in 't Veld, A. Kohlmeyer, S.G. Moore, T.D. Nguyen, R. Shan, M. J. Stevens, J. Tranchida, C. Trott, S.J. Plimpton, LAMMPS - a flexible simulation tool for particle-based materials modeling at the atomic, meso, and continuum scales, Comput. Phys. Commun. 271 (2022) 108171.
[26] A. Stukowski, Visualization and analysis of atomistic simulation data with OVITO-the open visualization tool, Modell. Simulat. Mater. Sci. Eng. 18 (1) (2010) 015012.
[27] Y. Wang, J. Xu, Y. Ootani, S. Bai, Y. Higuchi, N. Ozawa, K. Adachi, J.M. Martin, M. Kubo, Tight-binding quantum chemical molecular dynamics study on the friction and wear processes of diamond-like carbon coatings: effect of tensile stress, ACS Appl. Mater. Interface. 9 (39) (2017) 34396–34404.
[28] J. Hilbert, F. Mangolini, J.B. McClimon, J.R. Lukes, R.W. Carpick, Si doping enhances the thermal stability of diamond-like carbon through reductions in carbon-carbon bond length disorder, Carbon N.Y. 131 (2018) 72–78.
[29] Z. Chen, J. Wu, B. Su, Y. Wang, Temperature-structure-induced metastable structural transformation mechanism of the amorphous carbon film during friction, Tribol. Int. 191 (2024) 109112.
[30] T.-B. Ma, Y.-Z. Hu, L. Xu, L.-F. Wang, H. Wang, Shear-induced lamellar ordering and interfacial sliding in amorphous carbon films: a superlow friction regime, Chem. Phys. Lett. 514 (4) (2011) 325–329.
[31] X.H. Long, W. Setyawan, K.P. Tai, Y. Liu, M.S. Yu, Z.Q. Wang, N. Gao, X.L. Wang, Defect formation and bending properties in graphite under He atom implantation investigated by molecular dynamics method, Carbon N.Y. 191 (2022) 350–361.
[32] D. Hua, Q. Xia, W. Wang, Q. Zhou, S. Li, D. Qian, J. Shi, H. Wang, Atomistic insights into the deformation mechanism of a CoCrNi medium entropy alloy under nanoindentation, Int. J. Plastic. 142 (2021).
[33] W. Shao, Z. Shi, L. Rao, S. Zhang, X. Xing, Y. Zhou, Q. Yang, High-Temperature Sliding Friction Behavior of Amorphous Carbon Films: molecular Dynamics Simulation, Langmuir 36 (50) (2020) 15319–15330.
[34] J. Tersoff, New empirical approach for the structure and energy of covalent systems, Phys. Rev. B 37 (12) (1988) 6991–7000.
[35] L. Li, M. Xu, W. Song, A. Ovcharenko, G. Zhang, D. Jia, The effect of empirical potential functions on modeling of amorphous carbon using molecular dynamics method, Appl. Surf. Sci. 286 (2013) 287–297.
[36] L. Li, W. Song, J. Liu, Q. Liu, S. Wang, G. Zhang, Nanomechanical and nanotribological behavior of ultra-thin silicon-doped diamond-like carbon films, Tribol. Int. 94 (2016) 616–623.
[37] J.F. Ziegler, J.P. Biersack, The Stopping and Range of Ions in Matter, in: D. A. Bromley (Ed.), Treatise On Heavy-Ion Science: Volume 6: Astrophysics, Chemistry, and Condensed Matter, Springer US, Boston, MA, 1985, pp. 93–129.
[38] J. Qi, K. Komvopoulos, A molecular dynamics analysis of ion irradiation of ultrathin amorphous carbon films, J. Appl. Phys. 120 (12) (2016) 125311.
[39] J.T. Buchan, M. Robinson, H.J. Christie, D.L. Roach, D.K. Ross, N.A. Marks, Molecular dynamics simulation of radiation damage cascades in diamond, J. Appl. Phys. 117 (24) (2015) 245901.
[40] S. Li, W.T. Ye, Y.R. Shi, Q. Zhou, Y.N. Chen, T. Guo, Y.X. Liu, L.C. Zhang, H. F. Wang, Atomistic simulation and experimental verification of tribological behavior of high entropy alloy/graphene composite coatings, Surf. Coat. Technol. 467 (2023).
[41] J. Liang, H. Edelsbrunner, C. Woodward, Anatomy of protein pockets and cavities: measurement of binding site geometry and implications for ligand design, Prot. Sci. 7 (9) (1998) 1884–1897.
[42] X. Li, A. Wang, K.-R. Lee, Comparison of empirical potentials for calculating structural properties of amorphous carbon films by molecular dynamics simulation, Comput. Mater. Sci. 151 (2018) 246–254.
[43] N.A. Marks, Evidence for subpicosecond thermal spikes in the formation of tetrahedral amorphous carbon, Phys. Rev. B 56 (5) (1997) 2441–2446.
[44] D.R. McKenzie, D. Muller, B.A. Pailthorpe, Compressive-stress-induced formation of thin-film tetrahedral amorphous carbon, Phys. Rev. Lett. 67 (6) (1991) 773–776.
[45] C. Hardtke, W. Schilling, H. Ullmaier, Influence of particle bombardment on microstructure and internal-stresses of refractory-metal silicides on silicon, Nucl. Instrum. Method. Phys. Res. Sect. B-Beam Interact. Mater. Atom. 59 (1991) 377–381.
[46] Q. Liu, L. Li, Y.-R. Jeng, G. Zhang, C. Shuai, X. Zhu, Effect of interatomic potentials on modeling the nanostructure of amorphous carbon by liquid quenching method, Comput. Mater. Sci. 184 (2020) 109939.
[47] S. Lahkar, R. Ranganathan, Competing mechanisms govern the thermal rectification behavior in semi-stochastic polycrystalline graphene with graded grain-size distribution, Carbon N.Y. 218 (2024) 118638.
[48] H.-K. Kim, M. Lee, K.-R. Lee, J.-C. Lee, How can a minor element added to a binary amorphous alloy simultaneously improve the plasticity and glass-forming ability? Acta Mater. 61 (17) (2013) 6597–6608.
[49] J.E. Bloor, S. Gartside, Effect of hybridization changes on the bond energies of carbon - carbon single bonds, Nature 184 (4695) (1959) 1313. -1313.
[50] D.P. Hua, Q.S. Xia, W. Wang, Q. Zhou, S. Li, D. Qian, J.Q. Shi, H.F. Wang, Atomistic insights into the deformation mechanism of a CoCrNi medium entropy alloy under nanoindentation, Int. J. Plastic. 142 (2021).
[51] Q. Yu, X. Chen, C. Zhang, J. Tian, W. Deng, P. Huang, Extreme contact pressure-induced in-situ structural evolution of nanoclusters governing macroscopic superlubricity in a-C:H films, Carbon N.Y. 215 (2023) 118457.
[52] B. Schultrich, H.J. Scheibe, D. Drescher, H. Ziegele, Deposition of superhard amorphous carbon films by pulsed vacuum arc deposition, Surf. Coat. Technol. 98 (1) (1998) 1097–1101.
[53] F.J. Valencia, J. Santiago, R.I. González, R. González-Arrabal, C. Ruestes, M. Perez Díaz, M.A. Monclus, J. Molina-Aldareguia, P.D. Nuñez, F. Munoz, M. Kiwi, J. M. Perlado, E.M. Bringa, Nanoindentation of Amorphous Carbon: a combined experimental and simulation approach, Acta Mater. 203 (2021) 116485.
[54] H. He, M.F. Thorpe, Elastic properties of glasses, Phys. Rev. Lett. 54 (19) (1985) 2107–2110.
[55] W. Ye, Q. Zhou, Y. Shi, M. Xie, B. Chen, H. Wang, W. Liu, Robust wear performance of graphene-reinforced high entropy alloy composites, Carbon N.Y. 224 (2024) 119040.
[56] C. Zhong, H. Zhang, Q.P. Cao, X.D. Wang, D.X. Zhang, U. Ramamurty, J.Z. Jiang, On the critical thickness for non-localized to localized plastic flow transition in metallic glasses: a molecular dynamics study, Scr. Mater. 114 (2016) 93–97.
[57] Q. Jia, W. He, D. Hua, Q. Zhou, Y. Du, Y. Ren, Z. Lu, H. Wang, F. Zhou, J. Wang, Effects of structure relaxation and surface oxidation on nanoscopic wear behaviors of metallic glass, Acta Mater. 232 (2022) 117934.
[58] N. Du, X. Wei, X. Li, Z. Chen, S. Lu, J. Ding, C. Feng, K. Chen, J. Qiao, D. Zhang, K.-R. Lee, T. Zhang, Friction reactions induced by selective hydrogenation of textured surface under lubricant conditions, Friction 12 (1) (2024) 174–184.
[59] J. Goddard, H. Wilman, A theory of friction and wear during the abrasion of metals, Wear 5 (2) (1962) 114–135.
[60] Q. Jia, Q. Xia, Q. Zhou, Y. Wang, Y. Ren, Y. Meng, H. Wang, F. Zhou, Nanoscopic tribological characteristics of a cryogenically cycled Zr-based metallic glass, Sci. China: Phys. Mech. Astron. 67 (6) (2024).
[61] J. Ding, S. Lu, Z. Chen, X. Wei, H. Zhang, P. Guo, C. Feng, K. Chen, K.-R. Lee, X. Li, Synergistic lubrication of diamond-like carbon and poly-α-olefin oil: coupled dependence on oil viscosity and applied load, Ceram. Int. (2024).

[62] R. Brittain, T. Liskiewicz, A. Morina, A. Neville, L.Q. Yang, Diamond-like carbon graphene nanoplatelet nanocomposites for lubricated environments, Carbon N Y 205 (2023) 485–498.
[63] W.H. Zhuang, X.Q. Fan, W. Li, H. Li, L. Zhang, J.F. Peng, Z.B. Cai, J.L. Mo, G. G. Zhang, M.H. Zhu, Comparing space adaptability of diamond-like carbon and molybdenum disulfide films toward synergistic lubrication, Carbon N.Y. 134 (2018) 163–173.
[64] T.-B. Ma, L.-F. Wang, Y.-Z. Hu, X. Li, H. Wang, A shear localization mechanism for lubricity of amorphous carbon materials, Sci. Rep. 4 (1) (2014) 3662.
[65] R.Q. Mao, X.W. Cui, J.L. Hao, S.Z. Zhao, S. Hou, F.L. Lan, Y.B. Li, L.F. Deng, H. Li, Densification and surface carbon transformation of diamond powders under high pressure and high temperature, Mater. (Basel) 17 (3) (2024).
[66] Y. Suzuki, T. Arai, S. Kawaguchi, M. Taniguchi, K. Inoue, K. Akikubo, R. Suzuki, M. Tachibana, Raman study on the pressure-induced phase transformation of nanographite at room temperature, Carbon N.Y. 225 (2024) 119075.
[67] P. Zhang, J. Fan, Y. Wang, Y. Dang, S. Heumann, Y. Ding, Insights into the role of defects on the Raman spectroscopy of carbon nanotube and biomass-derived carbon, Carbon N.Y. 222 (2024) 118998.
[68] X. Chen, C. Zhang, T. Kato, X.-a. Yang, S. Wu, R. Wang, M. Nosaka, J. Luo, Evolution of tribo-induced interfacial nanostructures governing superlubricity in a-C:H and a-C:H:Si films, Nat. Commun. 8 (1) (2017) 1675.
[69] Z. Jiao, D. Hua, Q. Zhou, S. Li, D. Luo, H. Wang, W. Liu, Super-hard refractory high entropy alloy film with spinodal decomposition, J. Mater. Sci. Technol. 213 (2025) 190–195.
[70] Y. Liao, R. Pourzal, M.A. Wimmer, J.J. Jacobs, A. Fischer, L.D. Marks, Graphitic tribological layers in metal-on-metal hip replacements, Science 334 (6063) (2011) 1687–1690.